JOURNAL OF ADVANCED E-ISSN: 2979-9759 2024 VOLUME ISSUE WWW.JAASCI.COM PIPRENSIP

#### 2024 • VOLUME 3 • ISSUE 1

**Editor-in-Chief** 

Özgür ÖZTÜRK Kastamonu University, TÜRKİYE

**Associate Editors** 

Gürcan YILDIRIM Bolu Abant İzzet Baysal University, TÜRKİYE

Serap SAFRAN Ankara University, TÜRKİYE

**Technical Editors** 

Yiğit TAŞTAN Kastamonu University, TÜRKİYE Büşra TAŞTAN Prensip Publishing, TÜRKİYE Sedat KURNAZ Kastamonu University, TÜRKİYE

**Language Editor** 

Gürcan YILDIRIM Bolu Abant İzzet Baysal University, TÜRKİYE

**Editorial Board** 

Ali GENCER Ankara Univesity, TÜRKİYE

Cabir TERZİOĞLU Bolu Abant İzzet Baysal University, TÜRKİYE

Germán F. de la FUENTE Zaragoza University, SPAIN Yasuharu KAMIOKA ColdTech LLC, JAPAN

Kazuhiro KAJIKAWA Sanyo-Onoda City University, JAPAN

Shinji MASUYAMA National Institute of Technology, Oshima College, JAPAN

Ahmet Tolga TAŞÇI Kastamonu University, TÜRKİYE

Ali BOZBEY TOBB University of Economics and Technology, TÜRKİYE

Şükrü ÇELİK Sinop University, TÜRKİYE

Hakan YETİŞ Bolu Abant İzzet Baysal University, TÜRKİYE

Haluk KORALAY Gazi University, TÜRKİYE Şükrü ÇAVDAR Gazi University, TÜRKİYE Selim ACAR Gazi University, TÜRKİYE

Mehmet Ali AKSAN Malatya İnönü University, TÜRKİYE Hakan GÜNGÜNEŞ Çorum Hitit University, TÜRKİYE

Mustafa AKDOĞAN Bolu Abant İzzet Baysal University, TÜRKİYE

Lütfi ARDA Bahçeşehir University, TÜRKİYE

Murat OLUTAŞ Bolu Abant İzzet Baysal University, TÜRKİYE

Osman ÇİÇEK Kastamonu University, TÜRKİYE Hanifi ÇİNİCİ Gazi University, TÜRKİYE

Rıfkı TERZİOĞLU Bolu Abant İzzet Baysal University, TÜRKİYE

Salih GÖRGÜNOĞLU Kastamonu University, TÜRKİYE
Abdulkadir KARACI Samsun University, TÜRKİYE
Faruk ERKEN Kastamonu University, TÜRKİYE
Ali Burak ÖNCÜL Kastamonu University, TÜRKİYE

**Cover Design** 

Sedat KURNAZ Kastamonu University, TÜRKİYE

jaasci.com jadvappsci@gmail.com prensip.gen.tr info@prensip.gen.tr

Journal of Advanced Applied Sciences is a peer-reviewed scientific journal published by Prensip Publishing twice a year.

Use of any material hereunder requires a citation to Journal of Advanced Applied Sciences.



## 2024 • VOLUME 3 • ISSUE 1

## TABLE OF CONTENTS

RESEARCH ARTICLES	Pages
Theoretical Investigation of Mechanical and Electronic Properties of Hexagonal BaB <sub>2</sub>	
Cihan Parlak	1-5
Purity Detection of Some Liquids by Using Reflection Values Based on	
Metamaterial Sanam Movazzafgharehbagh, Faruk Karadağ	6-14
The Structural Examination of Fe/(Cu/Nb)/MgB <sub>2</sub> Multifilament Wires During Cold	
Forming Process  Doğan Avcı, Hakan Yetiş, Fırat Karaboğa, İbrahim Belenli	15-22
The Design and the Application of Off-Grid Solar Power System for a House in	
Kastamonu Selcuk Emiralioglu, Secil Karatay, Faruk Erken	23-31
Frequency Dependent Negative Dielectric Behavior in Parylene C Based Composite Films	
Utku Guduloglu, Sedat Kurnaz, Turgay Seydioglu, Gizem Bekar, Ozgur Ozturk	32-39





e-ISSN: 2979-9759



#### RESEARCH ARTICLE

# Theoretical Investigation of Mechanical and Electronic Properties of Hexagonal BaB<sub>2</sub>

Cihan Parlak<sup>™</sup> •



Bolu Abant İzzet Baysal University, Faculty of Arts and Sciences, Department of Physics, Bolu/Türkiye

#### ARTICLE INFO

#### **Article History**

Received: 24.10.2023 Accepted: 10.01.2024 First Published: 06.05.2024

#### **Keywords**

Ab initio calculations Elastic properties Electronic structure Superconductors



#### **ABSTRACT**

A comprehensive investigation of the electronic and mechanical properties in the hexagonal BaB2 binary system using state of the art first-principles computational techniques is critical for an in-depth understanding of the fundamental properties unique to this binary system. In this context, we derived elastic constants using the metric-tensor formulation, which allowed us to find important mechanical properties such as Bulk Modulus, Shear Modulus, and Vickers's hardness which are fundamental mechanical quantities. Also, this research includes a detailed analysis of the electronic band structures and a study comparison of Fermi surface topologies. The charge density at the Fermi level (N(E<sub>F</sub>)), which is very important in superconductivity theories, was found to be 1.43 states/eV.uc. Furthermore, we have explored whether there exists a close relationship between these properties and the superconducting behavior of the BaB2 material. Nevertheless, our calculations unequivocally demonstrate that the information derived from electronic band structures and Fermi surfaces alone is insufficient for a comprehensive explanation of the superconductivity phenomenon observed in such materials.

#### Please cite this paper as follows:

Parlak, C. (2024). Theoretical investigation of mechanical and electronic properties of hexagonal BaB2. Journal of Advanced Applied Sciences, 3(1), 1-5. https://doi.org/10.61326/jaasci.v3i1.100

#### 1. Introduction

The revelation of superconductivity (SC) within MgB<sub>2</sub> (Nagamatsu et al., 2001), a member of the AlB<sub>2</sub>-type materials, featuring a critical temperature (Tc) of approximately 39 K, has elicited considerable interest among the scientific community. AlB<sub>2</sub>-type structures, recognized for their exceptional attributes encompassing the electron-phonon pairing mechanism, electronic properties, superconductivity, and lattice dynamics, have been a focal point of recent research endeavors.

Although extensive investigations have been conducted on most materials within the AlB<sub>2</sub>-type structure, hexagonal BaB<sub>2</sub> has received relatively limited theoretical attention (Alarco et al., 2015). This scarcity of research may be attributed to the fact that hexagonal BaB<sub>2</sub> has not yet been experimentally synthesized. Nonetheless, this hypothetical material exhibits substantial promise as a high-temperature superconductor (HTS). In light of this, our proposal aims to comprehensively characterize BaB2 and unveil its mechanic and electronic properties. The ability to calculate the fundamental properties of materials from first-principles calculations has emerged in recent years as an increasingly attractive avenue of research, allowing reliable prediction of a material's properties before experimental verification. This is becoming particularly important in the study of superconductivity (Boeri & Bachelet, 2019; Parlak, 2021).

E-mail address: cihanparlak@gmail.com



1

<sup>&</sup>lt;sup>™</sup> Correspondence

This paper is structured as follows: In Part 2, we elucidate our computational methodologies and associated parameters. Part 3.1 delves into an extensive analysis of lattice structure. Section 3.2 provides a concise portrayal of the electronic band structures of the compounds under investigation. Additionally, Section 3.3 furnishes comprehensive data on the elastic properties of these compounds. Our findings culminate in Section 4, offering a succinct recapitulation of our principal results.

#### 2. Materials and Methods

In this investigation, we conducted all computations by employing the ABINIT software (Gonze et al., 2020) in conjunction with the density functional theory (DFT) methodology. The generalized gradient approximation (GGA) was employed for the exchange-correlation functional. To ensure the attainment of convergence, a plane-wave kinetic energy cutoff parameter of 40 Hartree was determined as the optimal choice. K-point sampling for Brillouin zone integrations was achieved using a Monkhorst-Pack mesh with a 16x16x16 grid.

#### 3. Results and Discussion

#### 3.1. Lattice Properties

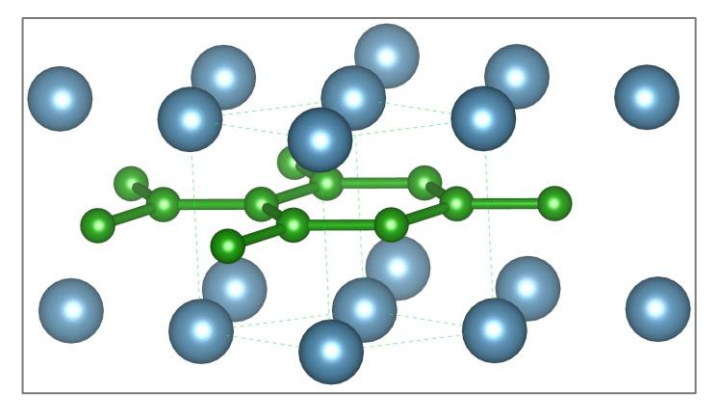


**Figure 1.** BaB2 lattice structure, the green color represents B atoms, and the blue color represents Ba atoms.

In the scope of this investigation, we embarked on the optimization of hexagonal di-boride  $BaB_2$  (Figure 1), a representative  $AlB_2$ -type material exhibiting the P6/mmm space group (no: 191). Within the well-defined  $AlB_2$ -type structural framework, Ba atoms are situated at the 1a (0,0,0) position, while B atoms are precisely situated at the 2d (1/3,2/3,1/2) Wyckoff positions (Parlak, 2020).

In our research, we have successfully acquired optimized lattice parameters for the  $BaB_2$  crystal structure, which are given as a=3.2842 Å and c=4.9551 Å, our results exhibit a commendable congruence with the relevant data available in the literature (Alarco et al., 2015). If we compare the lattice parameters of  $BaB_2$  with the most basic material of this family,

 $MgB_2$  (with a=3.086 Å and c=3.524 Å) (Nagamatsu et al., 2001). It is seen that the calculated lattice parameters of  $BaB_2$  are higher than those of  $MgB_2$ . This difference will play a role in the difference in basic mechanical and electronic properties.

#### 3.2. Electronic Properties

Possessing knowledge about the electronic band structure of a material affords insight into various physical characteristics of the material. This understanding is particularly significant in the context of superconducting materials, where the electronic structure exerts a direct and profound influence on superconducting properties. Notably, the superconducting transition temperature is acknowledged to exhibit a strong correlation with the electron density at the Fermi level, denoted as  $N(E_F)$  (Boeri & Bachelet, 2019).

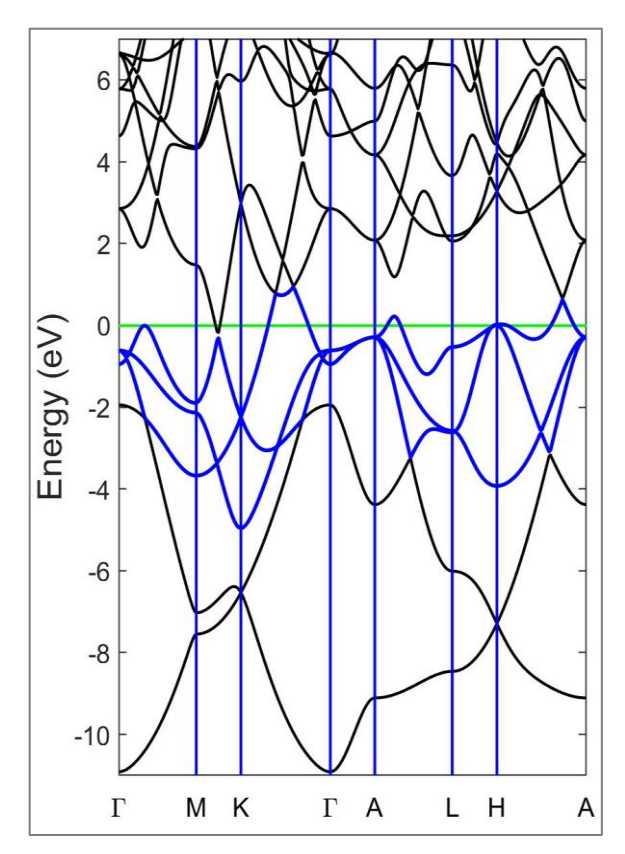


Figure 2. Electronic band structure of BaB2.

For this reason, in this study, the electronic band structure of the material was calculated in detail (Figure 2). As can be seen from the band structure, the material is completely metallic. One of the most important observations is the conical band structure located between the M-K points of the Brillouin region, very close to the Fermi level. This conical structure has been observed before in some AlB<sub>2</sub> structured materials (Xu et al., 2020) and is directly related to the topological semi-metal nature of the materials.

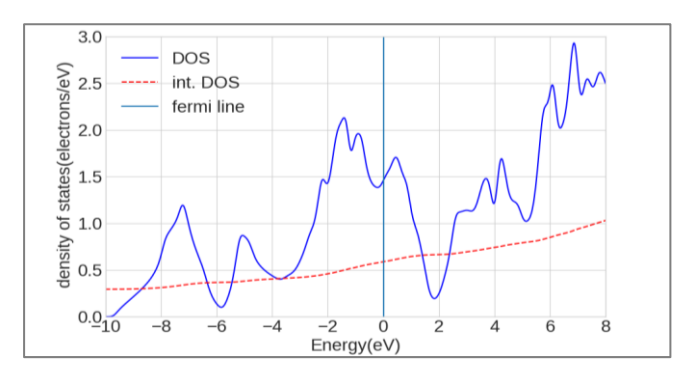
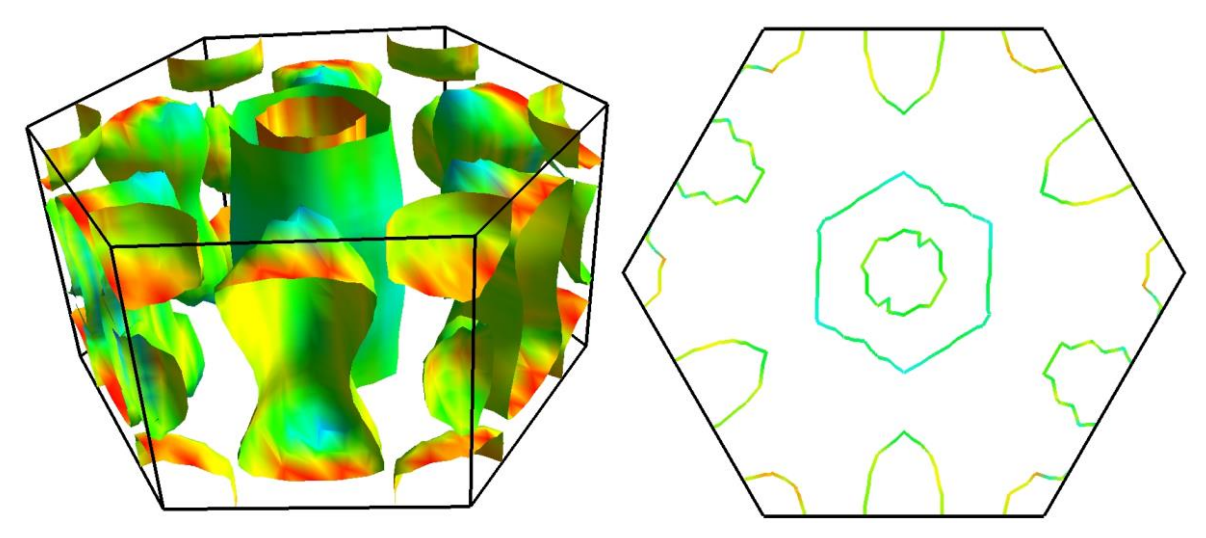


Figure 3. Total electron density of states (DOS).

We have given the electron density state of the material in Figure 3. The most striking feature here is the electron state density at the Fermi level is 1.43~States/eV.uc. And it can be said that this value is relatively high compared to  $MgB_2~(0.69~\text{states/eV.uc})$  (Choi et al., 2009)). From the perspective of superconductivity, although high electron state density at the Fermi level can be expected to cause high Tc, it should not be forgotten that electron-phonon interactions also play an extremely important role in such materials.



**Figure 4.** Fermi surface of BaB<sub>2</sub> and 2-D section view at the center of the Brillouin zone.

It would not be wrong to say that  $BaB_2$ 's Fermi surfaces consist of three independent surfaces (Figure 4), very similar to  $MgB_2$ . Two of them are along  $\Gamma$ -A and are hole-type cylindrical surfaces. The other is an electron-type surface with a 3-dimensional character near the borders of the Brillouin zone. In terms of Fermi surface topography,  $BaB_2$  does not have a very different structure from the general picture seen in other  $AlB_2$  structures and is even very similar to  $MgB_2$ .

#### 3.3. Mechanical Properties

The elastic tensor of a material serves as a fundamental tool for gaining deep insights into the material's reactivity under the influence of external forces. This information plays a pivotal role in dissecting the underlying bonding mechanisms and, in turn, enhances our grasp of the multifaceted mechanical and thermal attributes intrinsic to the material (DeJong et al., 2015). In the present investigation, we meticulously calculate the components of the elastic tensor employing the principles of linear response theory, as outlined by Hamann et al. (2005).

These elastic constants are instrumental in elucidating the material's nuanced response to diverse forms of deformation. For instance,  $C_{11}$ ,  $C_{12}$ , and  $C_{13}$  specifically characterize the material's behavior under axial deformations, while  $C_{33}$ ,  $C_{44}$ ,

and  $C_{66}$  are indicative of its response to shear deformations and other anisotropic features.

Furthermore, our findings unequivocally demonstrate that the computed elastic constants conform to the well-established Born criteria for a hexagonal lattice. These criteria, as expounded by Born et al. (1955), encompass conditions such as  $C_{11}>0$ ,  $C_{11}-C_{12}>0$ , and  $(C_{11}+C_{12})C_{33}-2(C_{13})2>0$ .

When comparing the elastic constants of BaB<sub>2</sub> ( $C_{11}$ =72.4,  $C_{12}$ =26.3,  $C_{13}$ =51.2,  $C_{33}$ =191.1,  $C_{44}$ =56.3,  $C_{66}$ =37.7 GPa) and MgB<sub>2</sub> ( $C_{11}$ =421,  $C_{12}$ =64,  $C_{13}$ =35,  $C_{33}$ =265,  $C_{44}$ =70,  $C_{66}$ =178 GPa (DeJong et al., 2015)), it's important to consider their mechanical properties and how they differ. These constants help scientists and engineers understand how materials respond to different types of deformation and provide insights into their mechanical behavior. Here's a comparison between the elastic constants of BaB<sub>2</sub> and MgB<sub>2</sub>:

- C<sub>11</sub> (Axial Stiffness): MgB<sub>2</sub> is significantly stiffer in the axial direction, indicating that it is more resistant to compression along this axis.
- C<sub>12</sub> (Shear Modulus, Shear Stiffness in XY Plane): MgB<sub>2</sub> has a higher shear modulus, suggesting that it is more resistant to shearing forces in the XY plane.

- C<sub>13</sub> (Shear Modulus, Shear Stiffness in XZ Plane): BaB<sub>2</sub> is stiffer in the XZ plane, indicating its resistance to shearing forces in that direction.
- C<sub>33</sub> (Axial Stiffness): MgB<sub>2</sub> is stiffer in the axial direction, making it more resistant to compression along this axis.
- C<sub>44</sub> (Shear Modulus, Shear Stiffness in YZ Plane): MgB<sub>2</sub> has a higher shear modulus in the YZ plane, indicating greater resistance to shearing forces in this direction.
- C<sub>66</sub> (Shear Modulus, Shear Stiffness in XZ Plane): MgB<sub>2</sub> is significantly stiffer in the XZ plane, making it more resistant to shearing forces in that direction.

In summary of elastic properties,  $MgB_2$  generally has much higher elastic constants compared to  $BaB_2$ , indicating that it is a stiffer and more rigid material. This means that  $MgB_2$  is better suited to withstand higher loads and deformations, especially in axial and shear directions. These differences in elastic constants can have significant implications for the material's mechanical properties and its performance in various applications. Scientists and engineers use these values to design and understand the behavior of materials in a wide range of contexts, from structural engineering to materials science research.

By using the ELATE software (Gaillac et al., 2016), the Voigt–Reuss–Hill approximation (Hill, 1952) can be used for the calculation of some important mechanical constants such as the Bulk (B), Young (E), and Shear (G) moduli. One can see the numerical values in Table 1.

**Table 1.** Calculated elastic constants  $(C_{ij})$ , bulk (B) and shear (G) moduli, Young moduli (E), compressibility  $(\beta, \text{ in } GPa^{-1})$ , the Pugh's indexes (G/B), Poisson's ratio  $(\upsilon)$ , Zener anisotropy factor (A), Universal elastic anisotropy index  $(A^u)$ .

Parameter	Pre. Study	MgB <sub>2</sub> <sup>a</sup>
B <sub>v</sub>	65.91	152.78
$G_{v}$	46.81	128.47
$\mathbf{B_r}$	49.36	144.09
$G_{r}$	42.52	106.24
В	57.64	148.43
G	44.67	117.35
β	0.0173	0.0067
G/B	0.77	0.79
E	106.49	278.83
υ	0.19	0.18
A	2.44	0.39
$\mathbf{A}^{\mathbf{u}}$	0.84	1.10

<sup>&</sup>lt;sup>a</sup> (DeJong et al., 2015)

Among the fundamental mechanical design parameters, the bulk modulus, defines a material's resistance to compression. In the current study, the Voigt bulk modulus value is approximately calculated to be 65.91~GPa, while the Reuss bulk modulus value for the  $BaB_2$  material is obtained to be approximately 49.36~GPa. It is clearly seen that both values are much lower than the values given in the table for  $MgB_2$ . These values characterize how effectively the material resists compressive forces.

The Vickers hardness ( $H_{\nu}$ ) parameter of the compound was determined using the microhardness empirical model proposed by Chen and colleagues (Chen et al., 2011). Microhardness is a well-established metric that offers valuable insights into both the elastic and permanent plastic deformations exhibited by the studied compound.

Our findings reveal that at zero pressure, the microhardness parameter are 10.70 GPa (Chen et al., 2011 formulation) and 18.94 GPa (Tian et al., 2012 formulation), indicating a relatively higher resistance to plastic deformation. These observations provide valuable information about the material's response to mechanical stress and have implications for its performance in various applications.

#### 4. Conclusion

In conclusion, our investigation into the electronic and mechanical properties of hexagonal BaB<sub>2</sub>, an AlB<sub>2</sub>-type material with P<sub>6/mmm</sub> symmetry, has yielded valuable insights into the fundamental characteristics of this compound. We successfully optimized the lattice parameters, In the realm of electronic properties, our study of the electronic band structure revealed that BaB2 is a metallic material with a distinctive conical band structure near the Fermi level, reminiscent of other AlB<sub>2</sub> structured materials. The electron density at the Fermi level, N(E<sub>F</sub>), was found to be 1.43 States/eV.uc., a relatively high value compared to MgB2, indicating potential for superconductivity, though electron-phonon interactions must also be considered. Moreover, the analysis of Fermi surface topography indicated that BaB2 exhibits three independent surfaces, similar to MgB2, further aligning it with the broader AlB<sub>2</sub> family.

In terms of mechanical properties, we have meticulously calculated the elastic constants, providing critical insights into BaB<sub>2</sub>'s reactivity to various forms of deformation. Our results affirm that these computed elastic constants adhere to the well-known Born criteria's for a hexagonal lattice. The Voigt bulk modulus, an essential mechanical parameter, was found to be 65.91 GPa, indicating BaB<sub>2</sub>'s resistance to compression. Additionally, the microhardness parameter, obtained through empirical models, exhibited a notable resistance to plastic deformation at zero pressure.

In summary, our study advances our understanding of BaB2's fundamental properties, offering a comprehensive view of its electronic and mechanical behavior. These findings provide a foundation for further exploration of its potential

applications, including its possible role in superconductivity, and underscore the importance of careful materials characterization and computational modeling in materials science research.

#### **Conflict of Interest**

The author has no conflict of interest to declare.

#### References

- Alarco, J. A., Talbot, P. C., & Mackinnon, I. D. R. (2015). Phonon anomalies predict superconducting T c for AlB<sub>2</sub> -type structures. *Physical Chemistry Chemical Physics*, *17*(38), 25090-25099. https://doi.org/10.1039/c5cp04402b
- Boeri, L., & Bachelet, G. B. (2019). Viewpoint: The road to room-temperature conventional superconductivity. *Journal of Physics: Condensed Matter*, *31*(23), 234002. <a href="https://doi.org/10.1088/1361-648X/ab0db2">https://doi.org/10.1088/1361-648X/ab0db2</a>
- Born, M., Huang, K., & Lax, M. (1955). Dynamical theory of crystal lattices. *American Journal of Physics*, 23(7), 474. https://doi.org/10.1119/1.1934059
- Chen, X. Q., Niu, H., Li, D., & Li, Y. (2011). Modeling hardness of polycrystalline materials and bulk metallic glasses. *Intermetallics*, 19(9), 1275-1281. https://doi.org/10.1016/j.intermet.2011.03.026
- Choi, H. J., Louie, S. G., & Cohen, M. L. (2009). Prediction of superconducting properties of CaB2 using anisotropic Eliashberg theory. *Physical Review B*, 80(6), 064503. https://doi.org/10.1103/PhysRevB.80.064503
- De Jong, M., Chen, W., Angsten, T., Jain, A., Notestine, R., Gamst, A., Sluiter, M., Ande, C. K., van der Zwaag, S., Plata, J. J., Toher, C., Curtarolo, S., Ceder, G., Persson, K. A., & Asta, M. (2015). Charting the complete elastic properties of inorganic crystalline compounds. *Scientific Data*, 2, 150009. <a href="https://doi.org/10.1038/sdata.2015.9">https://doi.org/10.1038/sdata.2015.9</a>
- Gaillac, R., Pullumbi, P., & Coudert, F. X. (2016). ELATE: An open-source online application for analysis and

- visualization of elastic tensors. *Journal of Physics: Condensed Matter*, 28(27), 275201. <a href="https://doi.org/10.1088/0953-8984/28/27/275201">https://doi.org/10.1088/0953-8984/28/27/275201</a>
- Gonze, X., Amadon, B., Antonius, G., Arnardi, F., Baguet, L., Beuken, J. M., ... & Zwanziger, J. W. (2020). The ABINIT project: Impact, environment and recent developments. *Computer Physics Communications*, 248, 107042. https://doi.org/10.1016/j.cpc.2019.107042
- Hamann, D. R., Wu, X., Rabe, K. M., & Vanderbilt, D. (2005). Metric tensor formulation of strain in density-functional perturbation theory. *Physical Review B*, 71(3), 035117. https://doi.org/10.1103/PhysRevB.71.035117
- Hill, R. (1952). The elastic behaviour of a crystalline aggregate. *Proceedings of the Physical Society. Section A*, 65(5), 349. https://doi.org/10.1088/0370-1298/65/5/307
- Nagamatsu, J., Nakagawa, N., Muranaka, T., Zenitani, Y., & Akimitsu, J. (2001). Superconductivity at 39 K in magnesium diboride. *Nature*, 410, 63-64. https://doi.org/10.1038/35065039
- Parlak, C. (2020). The physical properties of AlB2-type structures CaGa2 and BaGa2: An ab-initio study. *Physica B: Condensed Matter*, 576, 411724. https://doi.org/10.1016/j.physb.2019.411724
- Parlak, C. (2021). First-principles study of the electronic structure and elastic properties of SrGa2 under pressure. *Materials Today Communications*, 28, 102510. https://doi.org/10.1016/j.mtcomm.2021.102510
- Tian, Y., Xu, B., & Zhao, Z. (2012). Microscopic theory of hardness and design of novel superhard crystals. *International Journal of Refractory Metals and Hard Materials*, *33*, 93-106. https://doi.org/10.1016/j.ijrmhm.2012.02.021
- Xu, S., Bao, C., Guo, P. J., Wang, Y. Y., Yu, Q. H., Sun, L. L., Su, Y., Liu, K., Lu, Z. Y., Zhou, S., & Xia, T. L. (2020). Interlayer quantum transport in Dirac semimetal BaGa2. *Nature Communications*, 11, 2370. <a href="https://doi.org/10.1038/s41467-020-15854-0">https://doi.org/10.1038/s41467-020-15854-0</a>



PRENSIP
https://prensip.gen.tr

e-ISSN: 2979-9759

#### RESEARCH ARTICLE

# Purity Detection of Some Liquids by Using Reflection Values Based on Metamaterial

Sanam Movazzafgharehbagh<sup>™</sup> • Faruk Karadağ •

Çukurova University, Faculty of Science, Department of Physics, Adana/Türkiye

#### ARTICLE INFO

#### **Article History**

Received: 30.10.2023 Accepted: 10.01.2024 First Published: 06.05.2024

#### Keywords

Liquid samples Metamaterial Purity Sensor



#### ABSTRACT

The aim of this work is to design and fabricate a type of sensor based on Metamaterials. This structure determines the purity of Methanol and Ethanol mixture in the water by using the Octagonal form of a resonator and sample holder. The proposed structure has been employed in the 8-12 GHZ frequency band. The important thing in the work is the changes of the waveform at the resonance frequency. The output waveform of materials (reflection coefficient  $S_{11}$  or transmission coefficient  $S_{12}$ ) must be changed in the liner figure by considering the dielectric coefficient. We use copper for the metal layer and resonator and Isola IS680 (3.2DK) (lossy) for substrate layer. We simulate one unit cell of this Metamaterial sensor by CST microwave software and then achieve the results and evaluate them. Both the numerical and experimental tests, give the same outcomes and results and they will be in good agreement with each other. The proposed structure can be used in many applications where purity and determining of some materials might be necessary.

#### Please cite this paper as follows:

Movazzafgharehbagh, S., & Karadağ, F. (2024). Purity detection of some liquids by using reflection values based on metamaterial. *Journal of Advanced Applied Sciences*, *3*(1), 6-14. https://doi.org/10.61326/jaasci.v3i1.108

#### 1. Introduction

Metamaterials are unnatural materials that have different electromagnetic behaviors and show specific electromagnetic (EM) properties that cannot be found inherently in nature. The mentioned differences are negative refraction index, negative reflection, negative Doppler Effect, negative permittivity, and negative permeability. Metamaterials are usually applied in periodic constructions. It is a good way to design and fabricate by repeating structure with the unit cells. An array of unit cells may be used to get the structure. A unit cell is a combination of SRR and wire structure (Pendry et al., 1999). Metamaterials (MTMs) are defined as artificial electromagnetic (EM) materials that are rapidly developing as a research due to having

many potential application areas. Metamaterials are artificially engineered structures that provide extraordinary features such as backward propagation, negative permittivity and/or permeability. The left-handed materials with unusual electromagnetic properties (MTMs) were theoretically proposed by the Russian physicist Viktor Veselago in 1968 (Veselago, 1968) and then the history of these metamaterials started with the speculation on the existence of "substances with simultaneously negative values of  $\epsilon$  and  $\mu$ " (Caloz et al., 2004). After Victor Veselago's paper or proposal in 1967, more than 30 years elapsed and by trying the group of researchers in 2000, the first metamaterial was developed artificially with negative permeability and negative permittivity by using periodic metal resonators. So at the end of the 20th century, the

E-mail address: sanam.mov61@gmail.com



6

<sup>&</sup>lt;sup>™</sup> Correspondence

first metamaterial exhibit as expected by Veselago, but an artificial effectively homogeneous structure which was proposed by Smith and colleagues at University of California (Smith et al., 2000) and then MTMs were fabricated and began to be used in practical life with the help of Pendry et al. and Smith et al. The original approach proposed by Pendry et al. (1998), was to exploit the inductive response from structured nonmagnetic materials to obtain high-frequency magnetism. In the previous studies, for example, Transmission Line Integrated Metamaterial Based Liquid Sensor (Alkurt et al., 2018) and Chiral Metamaterial Sensor (CMS), Octagonal Shaped Metamaterial Absorber Based Energy (Bakır et al., 2018) have been designed, simulate and fabricate. Metamaterials have many application areas and different study topics due to a high potential of them and therefore application of Metamaterials have been searched and investigated by scientists interestingly. Metamaterials are using in many applications such as diffraction-limit breaking, invisible cloaks (Alitalo et al., 2007), antennas (Metamaterial can increase the gain and reduce the return loss and disadvantage of a patch antenna) (Zhu et al., 2005), filters, polarization converters, optics, cloaking (Pozar, 2004; Alitalo et al., 2007), super lensing, and sensor applications. We can enhance and increase the sensitivity and resolution of sensors with the help of Metamaterials. Metamaterial sensors are used in many fields like agriculture, biomedical etc. The aim of this study is to determine and detect the purity of Methanol's and Ethanol's mixture in the water by using the Octagonal form of resonator and sample holder. Disgned sensors in this study showed positive results in the processes of test. The difficulty of differentiating and detecting, fluids with each other is that the dielectric coefficients might be close to each other. We can see that the designed structure in simulation studies and experimental studies has been successfully exhibited as a sensor, performing the purity determination and detection process in real time, quickly and accurately.

#### 2. Materials and Methods

#### 2.1. Obtaining Parameters and Numerical Results

It is necessary to determine, dielectric constant and magnetic permeability coefficients. With the development of new technologies, the parameters such as refractive index, effective dielectric permittivity and effective magnetic permeability can be easily calculated by using the methods. There are different methods for obtaining these parameters. Each method has several advantages and disadvantages. However, there is the most advantageous method to calculate parameters such as dielectric constant and magnetic permeability coefficients from the s-parameters. An important technique of obtaining and calculating the parameters of Metamaterial, is characterizing EM properties of the medium. Numerical and experimental results are used to design new Metamaterials.-researchers can compare the numerical results

of simulation program with the obtaining parameters of the experimental method for structures. Each method includes limitations or specific constraints. By considering of these domains, measurements of the s-parameter of the transmission and reflection are performed with the help of Vector Network Analyzer. Then, by using the obtained S-parameters, the dielectric permittivity and magnetic permeability are calculated by appropriate methods.

The most commonly used methods for measuring S-parameters are listed below.

- Transmission line method
- Chiral method (reflection method)
- Resonance method

The most advantageous method for obtaining parameters such as the refractive index, effective dielectric permittivity and effective magnetic permeability from S-parameters is transmission/ reflection by line method, because in the transmission and reflection by line method, S-parameters are used directly and then parameters such as refractive index, effective dielectric permittivity and effective magnetic permeability are obtained another reason, these methods aren't time consuming and don't need many laboratory equipments.

The resonators at the front and back sides of the structure have symmetry and they could be placed at different angle to each other, in the chiral method (reflection method). There is a loop as a resonator with the gap in the Transmission line method to get strong resonance. CST is software that uses FDTD and FIT methods. The finite integration method is used to solve electromagnetic (EM) field problems in numerical terms. The finite integration method was developed in 1977 by Thomas Weiland (Weiland, 1977), and after many years of research, has been developed by researchers. This method works in the desired frequency domain. The basic approach of this method is to apply Maxwell's equations.

#### 2.2. Structures

In this section, the Metamaterial structure and the processes of works which are used in the study are described. The structure is simulated by using CST Microwave Studio program. We have investigated the structure and the designs of with octagonal shaped resonators-based purity of liquid. Relative dielectric constant and thickness, Isola IS680 (3.2DK) (lossy) material has been used for substrate of structure. Copper is used with the thickness of 0.035 mm as resonators with the electrical conductivity is  $5.8 \cdot 10^{-7}$  S/m. In order to reduce the losses on the selected material, the material of Isola IS680 (3.2DK, lossy) is particularly preferred as seen in Figure 1. The technical details and specifications for the mentioned structures are given in the following section and shown in Table 1 and Figures 2 and 3.

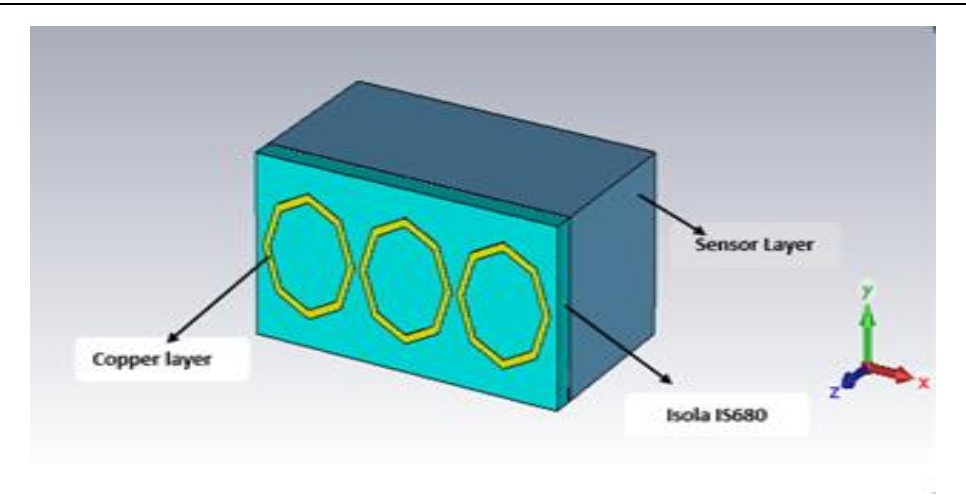


Figure 1. Type of materials use in octogonal-shaped resonator based purity of liquid.

Table 1. Specified Measurements of Octogonal Shaped Resonators to determine purity of liquid

Substrate x (mm)	Substrate y (mm)	Resonator (d1) mm	Resonator (d2) mm
22.86	10.16	2.68	2.30

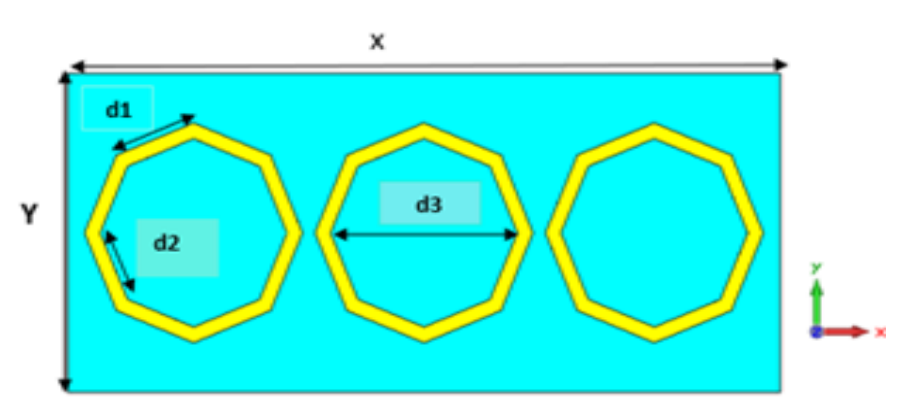


Figure 2. Dimension of octogonal shaped resonators to determine purity of liquid.

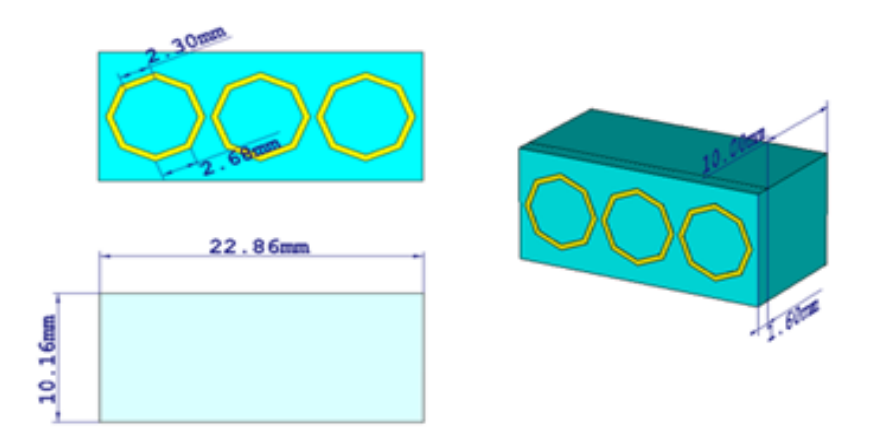


Figure 3. Unit cell's fabrication, front view, side and back view for octogonal-shaped resonator based purity of liquid.

#### 2.3. Defining Ports and Boundary Conditions

We have used waveguide port for this model as seen in Figure 4. Boundary conditions of unit cell, for the octogonal shaped resonator structure, in the  $X \ / \ Y \ / \ Z$  axes, have been selected and proposed, Electric (Et = 0) / Electric (Et = 0) /

Open Add Space respectively as shown in Figures 5 and 6. Axes and values are entered in the simulation program, for the characterization of the waveguide. The produced elements are located exactly inside the waveguide.

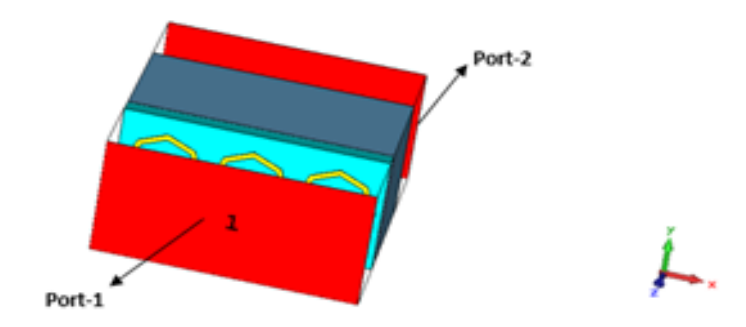
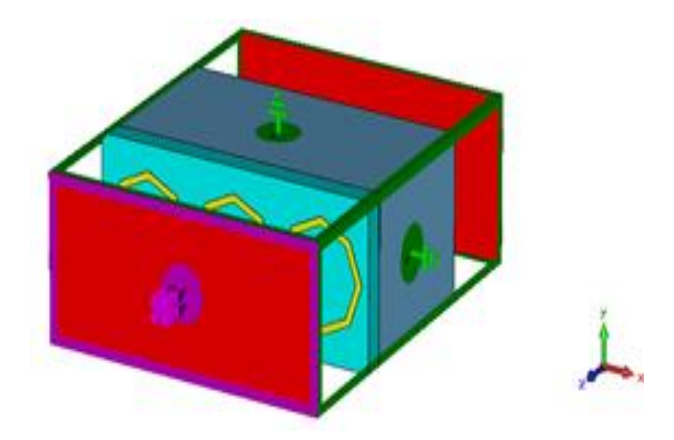


Figure 4. Defining of ports for octogonal-shaped resonator to determine purity of liquid structure.



**Figure 5.** Perspective view of boundary conditions applied for octogonal-shaped resonator.

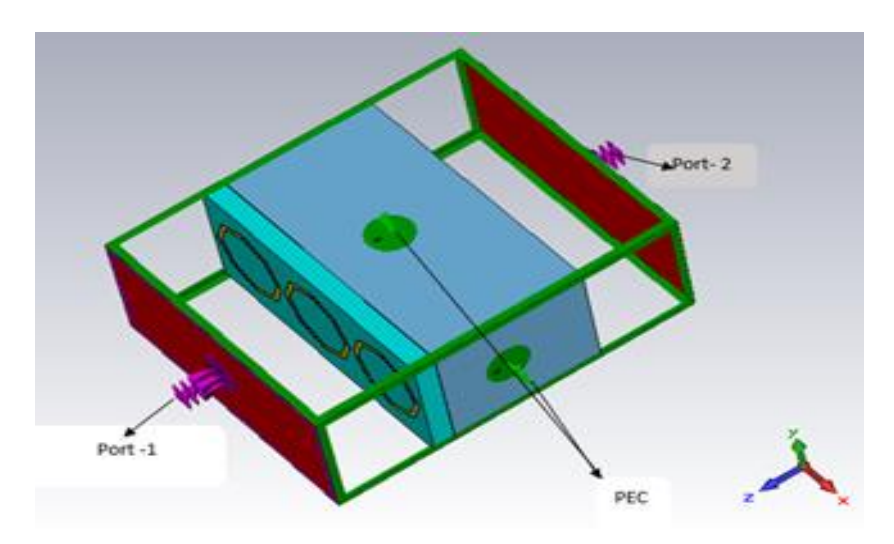


Figure 6. Boundry condition for octogonal-shaped resonator to determine purity of liquid structure.

The waveguide design, has a number of specification such as small construction, easy production and low cost. Waveguide dimensions are more important for operating frequency. In addition to the unit cell's boundary conditions, the reflection and transmission values are obtained by using the waveguide. Measurements are performed in TE wave mode using a network analyzer. As known, TEM wave cannot advance in waveguides. After measurement and simulation, it can be seen that experimental and numerical results are compatible with each other and there are very few differences. These differences are due to production, calibration and

material. In Figures 5 and 6 are shown that the Electric (Et = 0) boundary conditions are on the side and top walls. The resonators are arranged vertical to the axis, so that the direction of the magnetic field, as described in Faraday's law, is perpendicular to the resonators. All of these units are obtained by CST Microwave Studio program, which is an electromagnetic analysis program based on finite integral method. The Octogonal Shape Resonators are presented with different boundary conditions shown in Table 2. The boundary condition of the x and y axes are the same as with each other.

Figure 4 shows the design of the structure with boundary conditions.

**Table 2.** Boundary conditions applied for octogonal shape resonator for determine purity of liquid.

Boundary conditions	min	max
X	Electric (Et=0)	Electric (Et=0)
y	Electric (Et=0)	Electric (Et=0)
Z	Open (add space)	Open (add space)

#### 3. Results

# 3.1. Placed of Samples (Ethanol and Methanol's solution) in Sensor Layer

The reflection and transmission coefficients of the structure when the boundary condition is applied and the samples are placed are presented in Figures 7 and 8. These graphs are obtained in the case where the parameter is used in mm and Ethanol's solution as a sample placed in the sensor layer. The sensor layer, in Octogonal-Shaped Resonator Based purity of liquid, has 10 mm thickness and it is located just behind the Isola-is680 layer (substrate layer). By keeping the thickness of the sensor layer constant, the material of sensor, are modeled to be variable. Thus, parameters such as, dielectric constant can be detected.

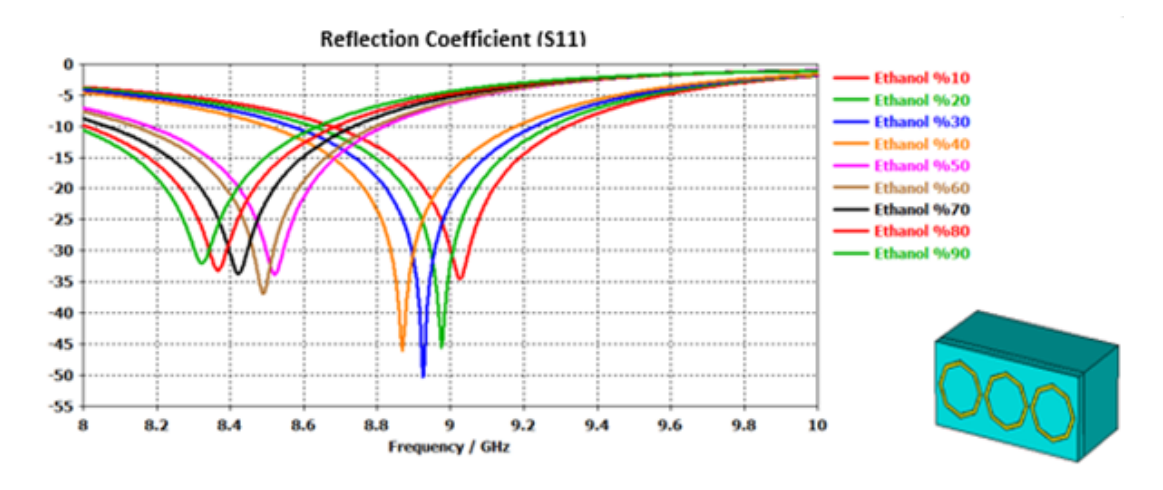


Figure 7. Reflection coefficient of ethanol's solution.

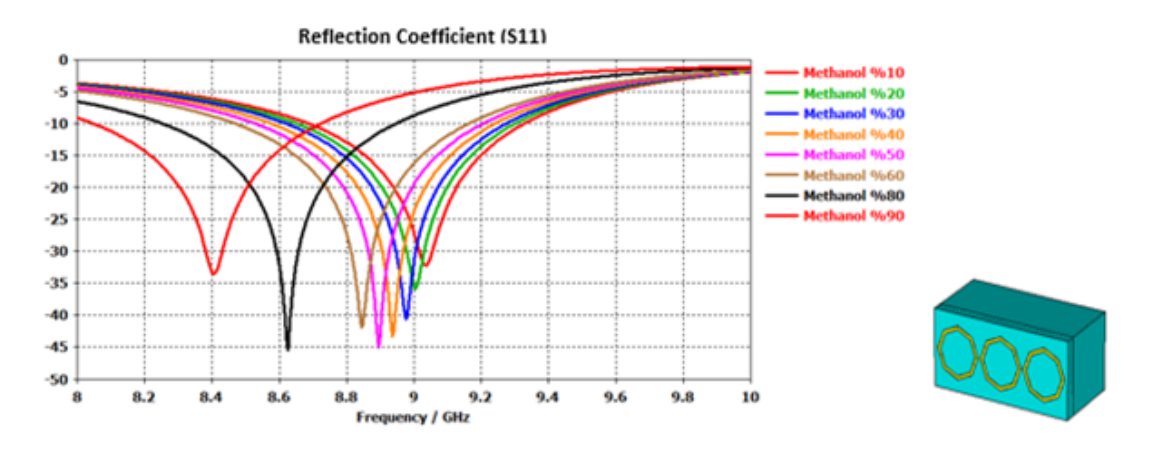


Figure 8. Reflection coefficient of methanol's solution.

When the reflection coefficient has checked and investigated, it has seen that there is a resonance at GHz levels in Octogonal-Shaped resonator Based purity of ethanol and methanol. Resonance Frequency of ethanol and methanol's solution in the Octogonal Resonator Based purity of liquid structure are given in Tables 3 and 4. However, when the

transmission coefficients are examined, it has seen that there is no resonance for the Octogonal-Shaped resonator structure. This is due to the fact that the capacitance cannot pull the resonance frequency to the selected band. Resonance values of Ethanol's solution are seen at different frequencies. In Figures 7 and 8, the transmission coefficient is unchanged while the reflection coefficient is shifted backwards.

**Table 3.** Resonance frequency of ethanol's solution in the octogonal resonator based purity of liquid structure.

=	
Ratio of Ethanol Mixture with Water	Resonance Frequency (GHZ)
Ethanol %10	9.024
Ethanol %20	8.976
Ethanol %30	8.924
Ethanol %40	8.868
Ethanol %50	8.520
Ethanol %60	8.488
Ethanol %70	8.420
Ethanol %80	8.368
Ethanol %90	8.324

**Table 4.** Resonance frequency of methanol's solution in the octogonal resonator based purity of liquid structure.

· ·	1 , 1
Ratio of Methanol Mixture with Water	Resonance Frequency (GHZ)
Methanol %10	9.036
Methanol %20	9.004
Methanol %30	8.976
Methanol %40	8.936
Methanol %50	8.896
Methanol %60	8.844
Methanol %70	8.755
Methanol %80	8.624
Methanol %90	8.408

# 3.2. Dielectric Constant of Samples (Ethanol and Methanol's Solution in Water)

The change of dielectric coefficients, with the values of the frequency, has been discussed in this section. The resonance frequency of the whole system will change when the dielectric constant of the sensor layer changes (Chieh-Sen & Yang, 2014). The dielectric constant varies according to environmental factors such as temperature, humidity or pressure. Electric Dispersion values are presented in Tables 5 and 6. According to the applying voltage, the values of the reflection coefficient (S11) have been changed. As seen in Figures 9 and 10 the dielectric coefficient affects the resonance frequency. When the temperature is increased, the resonance frequency of the reflection coefficient is linearly increased. This increase of value can be easily monitored by a network

analyzer. In sensor application, for the Octogonal-Shaped Resonator Based purity of liquid, the sensor plate is placed behind and back of the structure. Different materials could place on this sensor layer, but in this study, the applications of purity sensor will be investigated and explained in detail for two kind of sample. In addition, the sensor based Metamaterial structure can be used in other sensor applications if different materials are placed in the sensor layer. Material can be selected according to sensor parameters. Since the sensor parameter and selected samples changes the dielectric coefficient, the resonance frequency of the system will change. Dielectric coefficient for different ratio of materials placed on the sensor layer and measurements of the designed structure can be easily carried out by a network analyzer. Figures 9 and 10, shows the frequency value and electric dispersion of two samples. If we compare the changes of reflection coefficient (S11) with the dielectric coefficient of samples, it is seen that these changes are in a liner form according to ratio of Methanol solution.

**Table 5.** Electric dispersion of methanol in specific frequency (10 GHZ) in the structure.

Frequency (GHZ)	Ratio of Material	Dielectric Coefficient
10 GHZ	Methanol %10	55.46
10 GHZ	Methanol %20	46.80
10 GHZ	Methanol %30	40
10 GHZ	Methanol %40	32.34
10 GHZ	Methanol %50	26.41
10 GHZ	Methanol %60	20.67
10 GHZ	Methanol %70	14.98
10 GHZ	Methanol %80	11.19
10 GHZ	Methanol %90	8.93

**Table 6.** Electric dispersion of ethanol in specific frequency (10 GHZ) in the structure.

Frequency (GHZ)	Ratio of Material	Dielectric Coefficient	
10 GHZ	Ethanol %10	52.45	
10 GHZ	Ethanol %20	39.91	
10 GHZ	Ethanol %30	30.04	
10 GHZ	Ethanol %40	22.37	
10 GHZ	Ethanol %50	16.61	
10 GHZ	Ethanol %60	12.54	
10 GHZ	Ethanol %70	9.64	
10 GHZ	Ethanol %80	7.50	
10 GHZ	Ethanol %90	5.75	

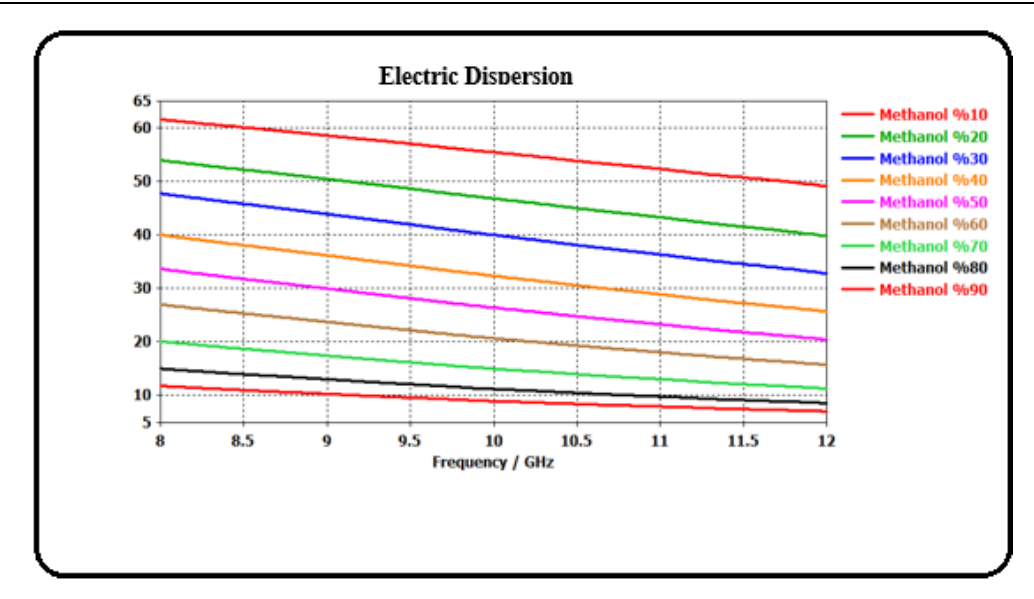


Figure 9. Frequency value and electric dispersion of methanol in the octogonal resonator based purity of liquid structure.

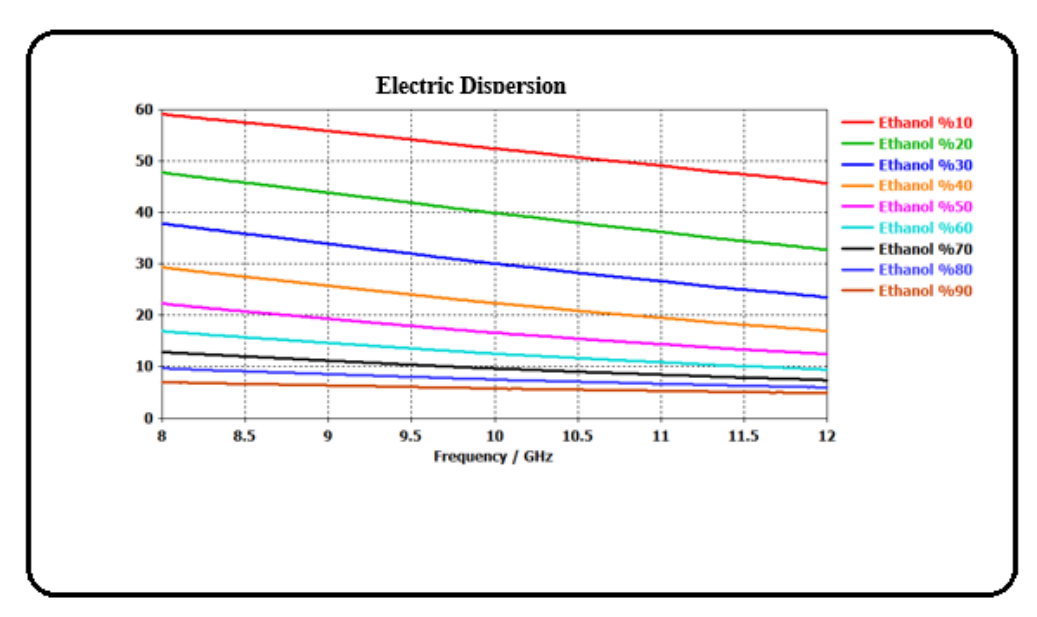


Figure 10. Frequency value and electric dispersion of ethanol in the octogonal resonator based purity of liquid structure.

# 3.3. Experimental Study of Octogonal-Shaped Resonator Based Purity of liquid Structure

In this study, reflection coefficients for the structure have been developed and obtained numerically and these results are proved by comparing them with experimental results. After performing numerical and experimental studies, the numerical results obtained by CST Microsoft program should be in good agreement with the experimental study results (Bakır, 2017). The purpose of selecting this structure is that it is easy to produce and can easily use in many fields such as determination of purity some liquid. The operating frequency is in the 8GHz-12GHz range. Figure 11 shows the details of the experimental study for Ethanol's solution. The experimental analysis results are presented in Figures 11 and 12.

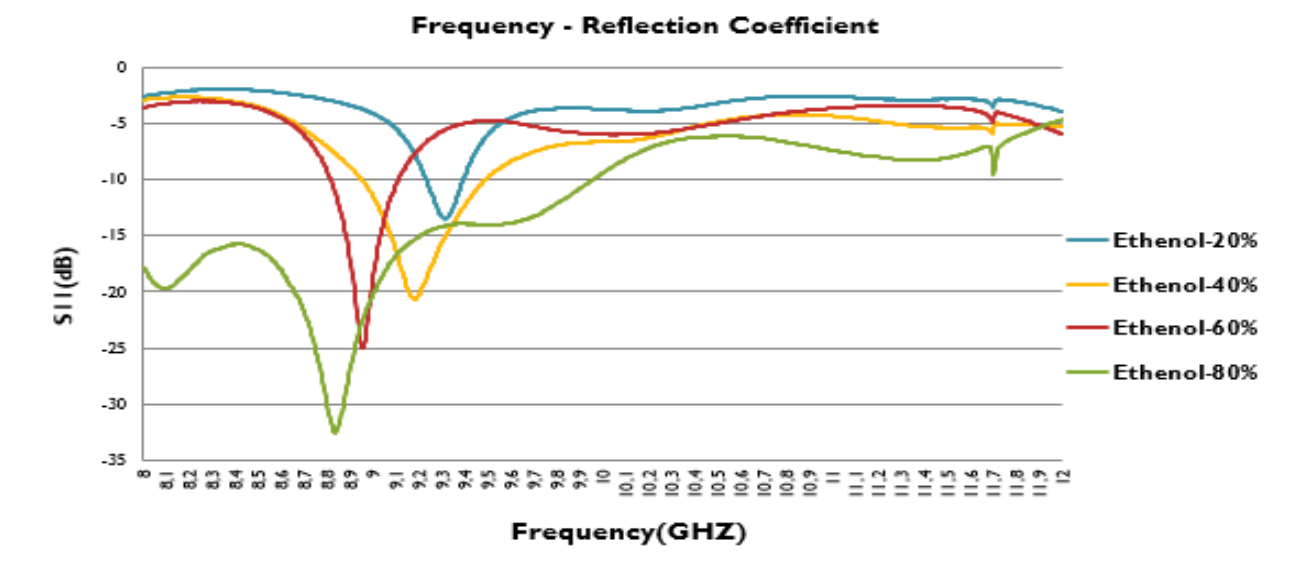


Figure 11. Experimental study results for ethanol's solution.

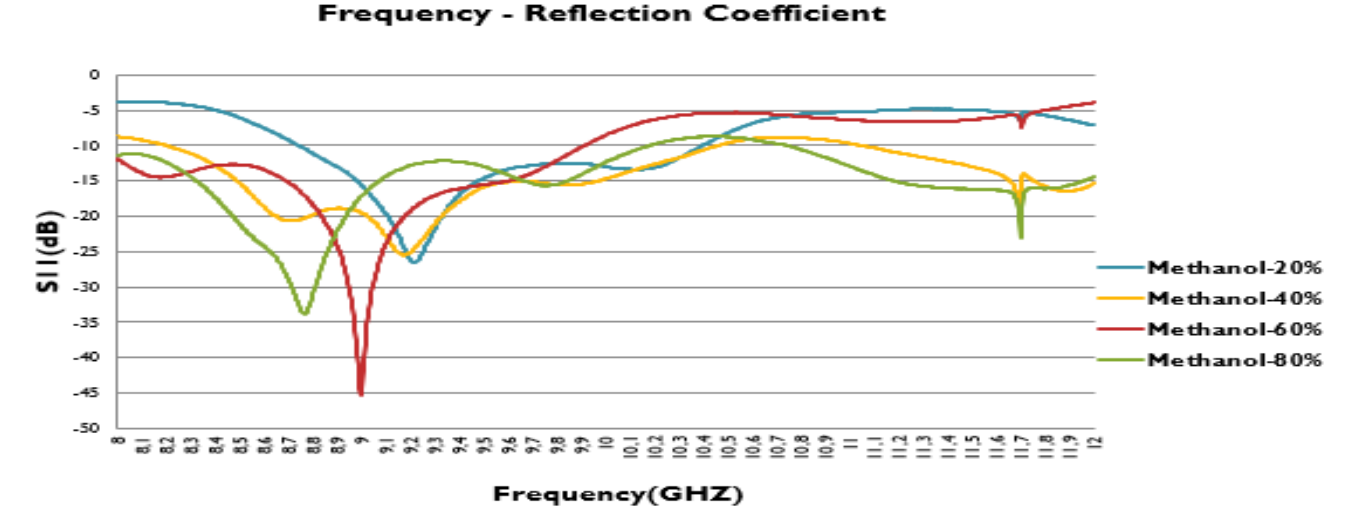


Figure 12. Experimental study results for methanol's solution.

#### 4. Discussion

The results, obtained from the simulation studies have evaluated and discussed with the experimental results for characterization of metamaterial structure. After measurement and simulation, it can be seen that experimental and numerical results are compatible with each other and there are very few differences. These differences are due to production, calibration and material. Electromagnetic characterization is very important for different applications of proposed structure. When electric and magnetic fields are focused in a certain direction, improved electrical and magnetic permeability occurs. Strong magnetic resonance is caused by inductance and capacitance effects between resonators. This indicates that the resonance is stimulated by the magnetic field. In this study, resonance frequencies for the periodic unit cell, electric field and surface current distributions is investigated and examined. If applications are related to the purity of liquid and

determination of liquid, they are carried out both experimentally and numerically. Reflection and transmission parameters (S-parameters) are both obtained with the CST Microwave Studio software based FIT method, as well as experimentally researched.

#### 5. Conclusion

The result of the Octogonal-Shaped Resonator Based purity of liquid for determination of liquid is investigated. In order to examine the simulation study results, we can see that the sensor we have designed successfully, perform real-time, fast, quick and accurate in the measurements as liquid detection sensors. It is observed that the resonance frequency changes in a linear way compared to the samples that we are examined. As a result of this linearity it is seen that there is a detection band width. In addition to these changes, it is proved that the values of the reflection coefficient (S11 parameter), according to results, can

be used to determine the purity of ethanol and methanol samples in the Octogonal-Shaped Resonator Based purity of liquid. It is observed that changing amount of ethanol and methanol will cause linear changes in the resonance frequency. Octogonal-Shaped Resonator Based purity of liquid sensor has low costs. We can measure and examine them with small amount of samples. When the results are examined, it could be seen that they give very sensitive results. The sensor in this study showed positive results in the processes of test.

#### Acknowledgment

The authors would like to thank Physics Department of Çukurova University and Electrical and Electronics Engineering Department of Iskenderun Technical University for providing any support and for the opportunity to publish this work.

#### **Conflict of Interest**

The authors declare that they have no conflict of interest.

#### **References**

- Alitalo, P., Luukkonen, O., Jylhä, L., Venermo, J., & Tretyakov, S. (2007). Transmission-line networks cloaking objects from electromagnetic fields. *IEEE Transactions on Antennas and Propagation*, *56*(2), 416-424. https://doi.org/10.1109/TAP.2007.915469
- Alkurt, F. Ö., Bağmacı, M., Karaaslan, M., Bakır, M., Altıntaş, O., Karadag, F., Akgöl, O., & Ünal, E. (2018). Detection behind a wall by using microwave techniques. *AIP Conference Proceedings*, 1935(1), 060002. <a href="https://doi.org/10.1063/1.5025980">https://doi.org/10.1063/1.5025980</a>
- Bakır, M. (2017). Electromagnetic-based microfluidic sensor applications. *Journal of the Electrochemical Society*, 164(9), B488-B494. https://doi.org/10.1149/2.0171712jes
- Bakır, M., Karaaslan, M., Unal, E., Karadag, F., Alkurt, F. Ö., Altıntaş, O., Dalgac, S., & Sabah, C. (2018). Microfluidic and fuel adulteration sensing by using

- chiral metamaterial sensor. *Journal of the Electrochemical Society*, 165(11), B475-B483. <a href="https://doi.org/10.1149/2.0231811jes">https://doi.org/10.1149/2.0231811jes</a>
- Caloz, C., Lai, A., & Itoh, T. (2004). Wave interactions in a left0handed mushroom structure. IEEE Antennas and Propagation Society Symposium. Monterey.
- Chieh-Sen, L., & Yang, C. L. (2014). Thickness and permittivity measurement in multi-layered dielectric structures using complementary split-ring resonators. *IEEE Sensors Journal*, 14(3), 695-700. <a href="https://doi.org/10.1109/JSEN.2013.2285918">https://doi.org/10.1109/JSEN.2013.2285918</a>
- Pendry, J., Holden, A., Robbins, D., & Stewart, W. (1998). Low frequency plasmons in thin-wire structures. *Journal of Physics: Condensed Matter*, 10, 4785-4809. https://doi.org/10.1088/0953-8984/10/22/007
- Pendry, J. B., Holden, A. J., Robbins, D. J., & Stewart, W. J. (1999). Magnetism from conductors and enhanced nonlinear phenomena. *IEEE Transactions on Microwave Theory and Techniques*, 47(11), 2075-2084. https://doi.org/10.1109/22.798002
- Pozar, M. (2004). Microwave engineering. John Wiley & Sons.
- Smith, D. R., Padilla, W. J., Vier, D. C., & Nemat, S. C. (2000). Composite medium with simultaneously negative permeability and permittivity. *Physical Review Letters*, 84(18), 4184-4187. https://doi.org/10.1103/PhysRevLett.84.4184
- Veselago, V. G. (1968). The electrodynamics of substances with simultaneously negative values of ε and μ. *Soviet Physics Uspekhi*, 10(4), 509-514. https://doi.org/10.1070/PU1968v010n04ABEH003699
- Weiland, T. (1977). A discretization model for the solution of maxwell's equations for six-component fields. *Electronics and Communications*, 31(3),116-120.
- Zhu, F., Lin, Q., & Hu, J. (2005). *A directive patch antenna* with a metamaterial cover. IEEE. Asia-Pacific Microwave Conference Proceedings (APMC). Suzhou.



e-ISSN: 2979-9759



#### RESEARCH ARTICLE

# The Structural Examination of Fe/(Cu/Nb)/MgB<sub>2</sub> Multifilament Wires During Cold Forming Process

Doğan Avcı<sup>1™</sup> • Hakan Yetiş<sup>2</sup> • Fırat Karaboğa<sup>3</sup> • İbrahim Belenli<sup>2</sup> •

#### ARTICLE INFO

#### **Article History**

Received: 06.12.2023 Accepted: 20.02.2024 First Published: 06.05.2024

#### **Keywords**

В

Cold forming

Mg

MgB2 wire

Superconductivity

Transport measurements



#### **ABSTRACT**

In this study, we have successfully produced a Fe-sheathed 6+1 multifilament wire using Cu/Nb/MgB $_2$  monocore wires. The mono filament wire was prepared using Mg+2B powder mixture by powder-in-tube method without any intermediate heat treatment. The powder mixture of the amorphous nano boron (PVZ Nano Boron, purity of 98.5%, particle sizes < 250 nm) and high purity Mg powder (PVZ Mg, purity of 99%, particle size 74 $\mu$ m) were used. The multifilament wire was produced using groove rolling and cold drawing machines. The geometrical form of the filaments was examined using wire pieces taken from the wire at different steps throughout the production process. Finally, the multifilament wires produced in two different diameters of 1.02 mm and 0.82 mm were investigated in terms of filament uniformity, crack formation, surface roughness, and electrical transport properties. The structural examination was done on Nb filaments after the Fe and Cu sheaths were etched using HCl and HNO $_3$  solution. The I – V measurements of the multifilament wires heat treated at 650 °C for 15, 30, 45, 60, and 240 minutes, and 700 °C for 60 minutes were carried out for the applied current up to 1 A at 25 K under various external magnetic field.

#### Please cite this paper as follows:

Avcı, D., Yetiş, H., Karaboğa, F., & Belenli, İ. (2024). The structural examination of Fe/(Cu/Nb)/MgB<sub>2</sub> multifilament wires during cold forming process. *Journal of Advanced Applied Sciences*, *3*(1), 15-22. https://doi.org/10.61326/jaasci.v3i1.127

#### 1. Introduction

Following the discovery that  $MgB_2$  is a superconductor, various forms of  $MgB_2$  have been fabricated, including bulk structures, thin films, tapes, and wires (Feng et al., 2003; Nakane et al., 2005; Xi, 2009; Koblischka et al., 2014). Among these,  $MgB_2$  in wire form stands out as a particularly promising superconducting material for magnet applications due to its utilization of cost-effective raw materials and its straightforward production processes (Vinod et al., 2007; Yao et al., 2010; Patel et al., 2014). In the realm of technological

applications, the production of long multifilament wires is mandatory to reduce AC losses (Jiawen et al., 2019). Various manufacturing techniques, such as the powder-in-tube (PIT) process and continuous tube filling forming (CTFF) process, have been employed in the production of  $MgB_2$  wire. The CTFF process allows the fabrication of long wires, but controlling the initial filling density is challenging (Suo et al., 2007; Tomsic et al., 2007). To advance the development of superconducting devices utilizing  $MgB_2$  wire, there is a need for multifilament wire created from high-density monofilaments to enhance the

E-mail address: davci.0209@gmail.com



<sup>&</sup>lt;sup>1</sup>TÜBİTAK National Metrology Institute, Quantum Metrology Laboratory, Kocaeli/Türkiye

<sup>&</sup>lt;sup>2</sup>Bolu Abant İzzet Baysal University, Faculty of Arts and Sciences, Department of Physics, Bolu/Türkiye

<sup>&</sup>lt;sup>3</sup>Bolu Abant İzzet Baysal University, Mehmet Tanrıkulu Vocational School of Health Services, Bolu/Türkiye

<sup>&</sup>lt;sup>™</sup> Correspondence

critical current density  $(J_c(B))$ . Investigating the structural properties of MgB2 filaments is crucial to advance the development of MgB<sub>2</sub> filaments. The deformations during the production process are highly effective on the electrical performance of MgB<sub>2</sub> wire (Goldacker et al., 2004a). Filament size, geometrical alignment, filament integrity, and sausage effects related to wire structure can be easily explored using the optical microscopy and scanning electron microscopy, but these methods are destructive. Masayoshi and Yuichi (2023) conducted a study involving an MgB2 wire with 18 filaments, utilizing X-ray computed tomography (CT) to observe deformations such as sausage effects and filament breakage points on the filament surfaces. X-ray CT is effective as a nondestructive method for detecting deformations, but it is not sufficient to definitely distinguish types of deformation, such as cracks or sausages.

In this study, we used an etching technique to understand the origin of deformations in the filaments. The 6 filament Fe/Cu/Nb/MgB $_2$  multifilament wire was produced using both cold drawing and rolling methods without any intermediate heat treatment. The iron (Fe) and copper (Cu) sheaths were selectively etched using a hydrochloric acid (HCl) and nitric acid (HNO $_3$ ) solution, to expose the niobium (Nb) filaments. We examined the deformities arising during the cold-forming process on Nb filaments for different wire diameters. The electrical performance of the multifilament superconducting wires was tested by R-T and I-V measurements.

#### 2. Materials and Methods

The mono-filament  $MgB_2$  wire used for making the multifilament wire was fabricated with Cu/Nb sheaths.

Amorphous nano-boron powder (98% purity, < 250 nm size) and magnesium powder (99% purity, 74-144 µm size) were mixed according to the stoichiometric ratio (Mg+2B) using ball milling for 3 hours (Agate ball ratio 1:4, 200 rpm). The prepared powder mixture was filled into Nb tube (outer/inner diameter: 8/5 mm), and the Nb tube was placed into a Cu tube (outer/inner diameter: 12/8.30 mm). The Cu/Nb/Mg+2B sample was drawn from 12 mm to 1.94 mm without any intermediate heat treatment. The six wire pieces were then cut from the monofilament wire and the pieces were placed into a Fe tube (outer/inner diameter: 8/6 mm) with a Cu rod having diameter of 1.94 mm. The Cu rod was used as a stabilizer at the center of the filaments. Finally, the multifilament wire was produced for two different diameters of 1.02 and 0.82 mm by using cold drawing and rolling machines without any intermediate heat treatment as represented in Figure 1. During the cold forming processes, some pieces with diameters of 3.62 mm, 2.71 mm, 2.32 mm, and 1.50 mm were cut from the multifilament wire for the surface examination of Nb filaments (see Figure 2). The electrical measurements were performed on the wires with diameters of 1.02 mm and 0.82 mm, which were heat treated at 650 °C for 15-30-45-60-240 min. and at 700 °C for 60 min. Resistivity  $(\rho - T)$  measurements were carried out between 10 and 45 K by applying 500 mA of DC current. The current-voltage (I - V) measurements were performed at 25 K under external magnetic field by applying a maximum 1 A DC current. Structural analyses were performed on the cross-sectional surface of the wires and the longitudinal section of Nb filaments by using optical microscopy before heat treatments.

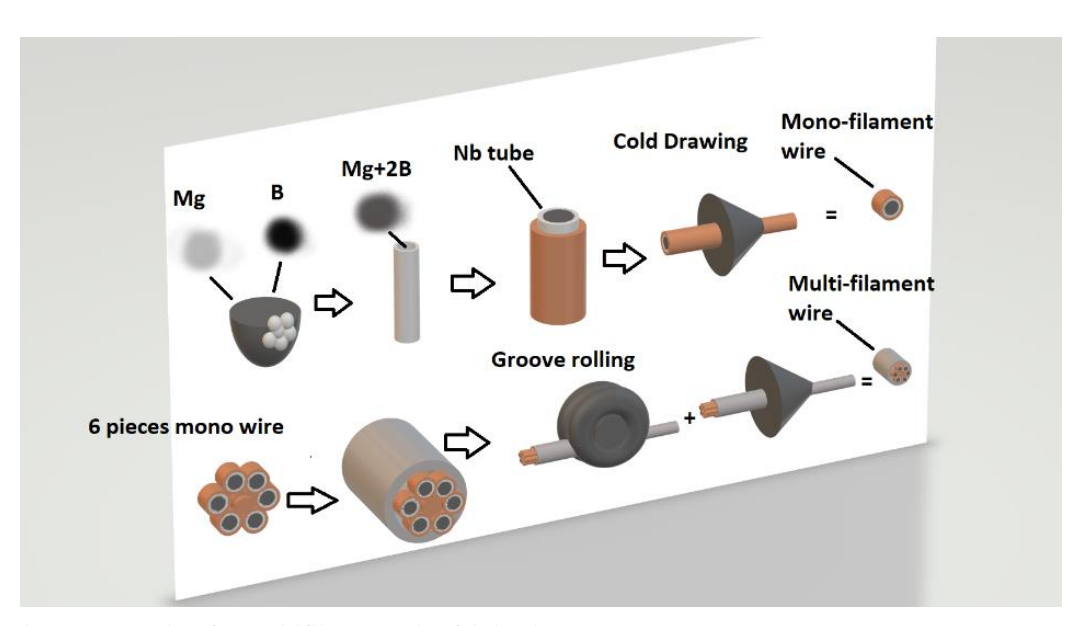
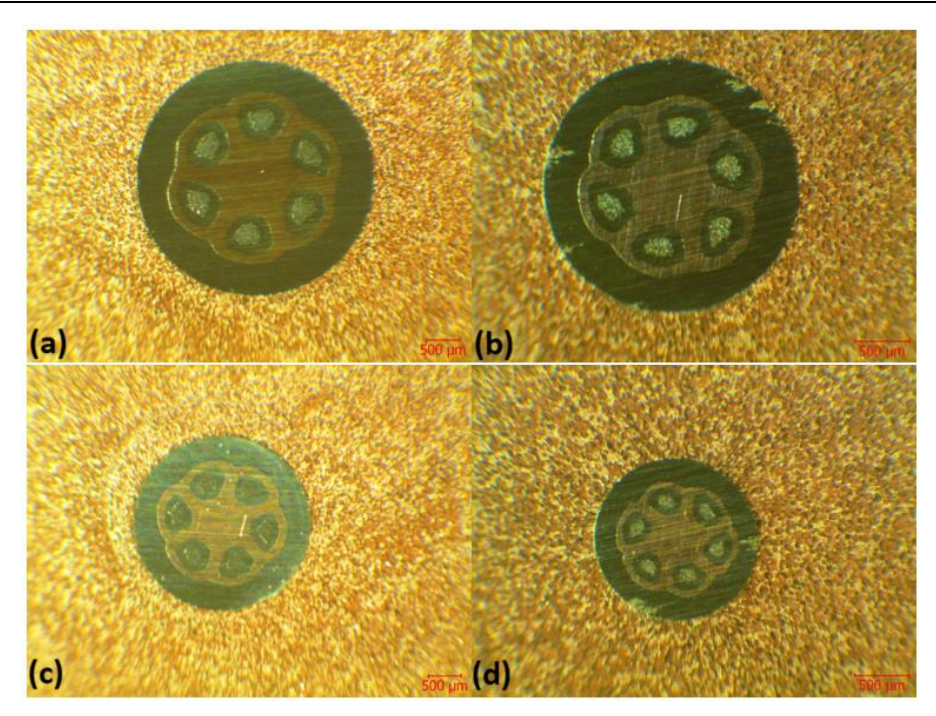


Figure 1. Schematic representation for multifilament wire fabrication.



**Figure 2.** Surface images of wire pieces cut in different diameters during the cold forming process. The wire diameters are (a) 3.62 mm, (b) 2.71 mm, (c) 2.32 mm, and (d) 1.50 mm, respectively.

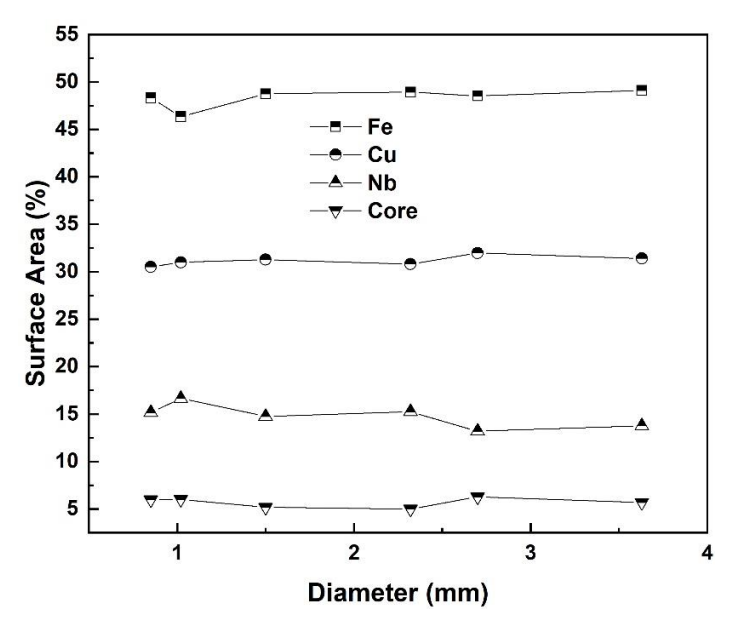


Figure 3. The percentage ratio of surface area of materials at different wire diameters.

The metallic cladding parts of the multifilament wires occupy 94% of the total cross-sectional area as shown in Figure 3. This also means that the superconducting MgB<sub>2</sub> content of the wire is only 6%. The fact that the cross-sectional areas of the core and metal components remain proportionally constant at different diameters is an indication that the extension/compression ratio is maintained.

#### 3. Results and Discussion

Figures 4(a) and (b) illustrate the  $\rho$  – T curves of Fe/Cu/Nb/MgB<sub>2</sub> multifilament wires heat treated at different

annealing temperature and time. It is seen from Figures 4(a) and (b), all wires showed transition from normal to superconducting state in self-magnetic field. The zero resistivity is achieved at temperatures between 34 K and 35 K for all wires. The inset graphs in Figures 4(a) and (b) indicate the presence of a sharp superconducting transition for all wires. The superconducting transition width ( $\Delta T$ ) was determined to be below 1 K. The wires heat treated at 650 °C for 1h or less have slightly lower  $T_{\rm c}$  values than wires heat-treated at 650 °C for 240 min. and 700 °C for 60 min. This difference in  $T_{\rm c}$  became more pronounced in wires with a diameter of 0.82 mm. The steep linear increase in normal state resistivity with increasing

temperature and the low  $\rho(40~{\rm K})$  value of 0.15  $\mu\Omega$ .cm are result of the high metallic content of the wires.

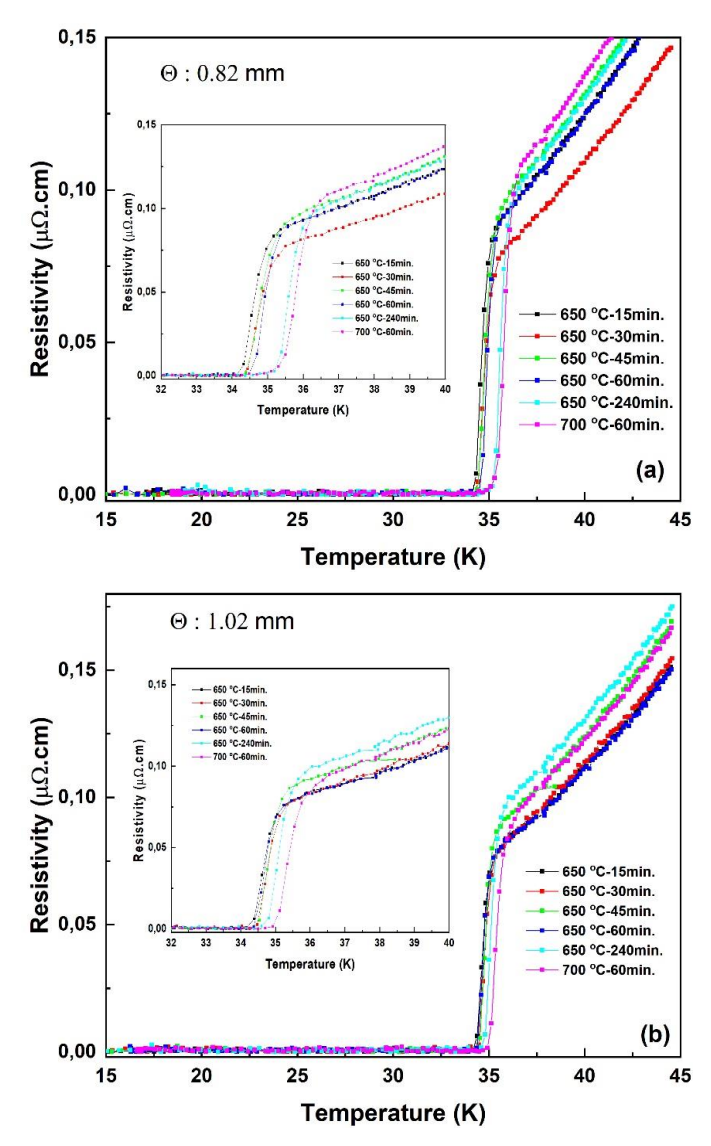


**Figure 4.** The resistivity vs. temperature curves of multifilament wires produced for two different diameters of (a) 0.82 and (b) 1.02 mm. The wires were heat treated under different conditions.

Figures 5(a) and (b) show the E-I curves obtained at 25 K under 3.75 T for the wires with diameters of 0.81 mm and 1.02 mm, respectively. Different sections of the multifilament wire were used for each E-I measurement. It is observed that there are some changes on the transport properties of Fe/Cu/Nb/MgB<sub>2</sub> multifilament wires annealed under different heat treatment conditions. It may be thought that the changes in  $I_c$  values may be caused by differences in heat treatment conditions, but this is not evident in the E-I measurements obtained with an applied current of 1 A. As seen in Figure 5(b), the  $I_c$  value of the wire annealed at 650 °C for 15 min. is the same as that of the wires annealed at 700 °C for 60 min. and 650 °C for 60 min. On the other hand, it is evident that the diameter of the wire directly influences its transport properties,

as decreasing wire diameter leads to an increase in core density. As seen in Figures 5(a) and (b), the  $I_c$  values of the wires under external magnetic field decreases when the wire diameter is reduced from 1.02 mm to 0.82 mm.

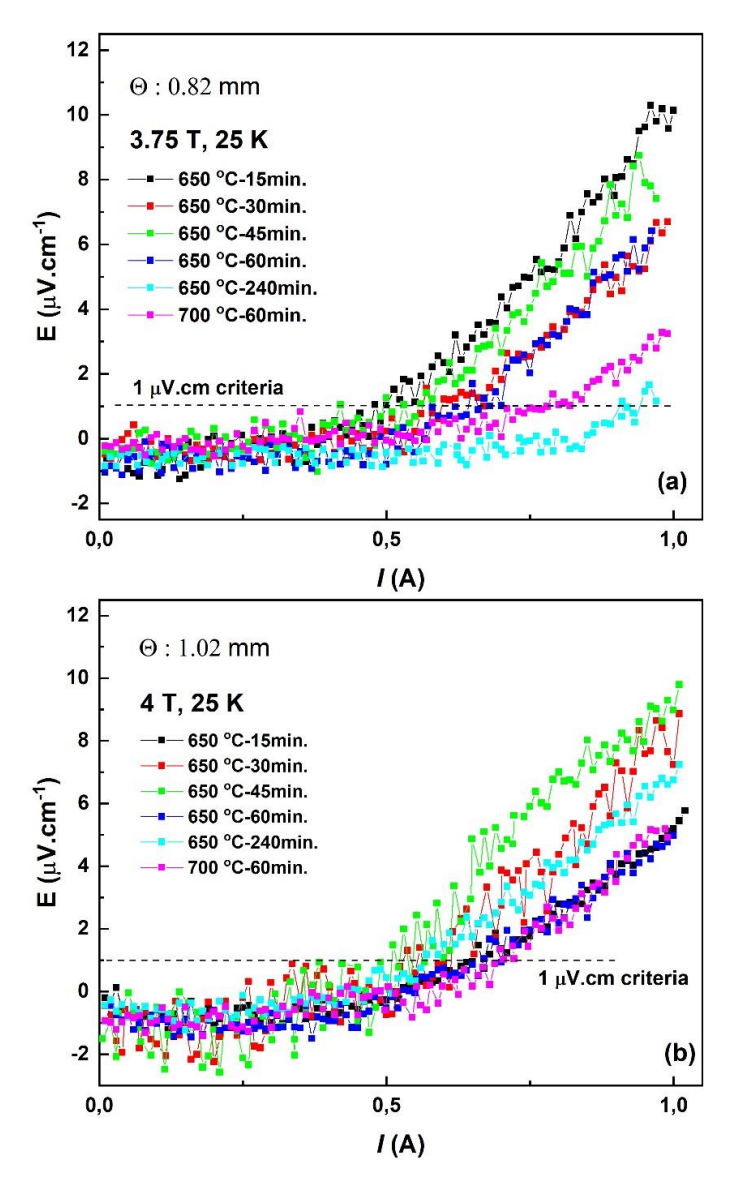


**Figure 5.** Electric field vs. current curves of multifilament wires with diameters of (a) 0.82 mm and (b) 1.02 mm. The wires were annealed at different temperature and time.

Images taken with an optical microscope from a single filament of multifilament wires with outer diameters of 0.82 mm and 1.02 mm subjected to different heat treatments are given in Figures 6 and 7, respectively. When the images are examined, the orange core regions in the wires show that MgB2 phase is successfully formed. It is seen that the use of large Mg particles results in the formation of a locally dense MgB2 structure, but also causes some unreacted boron regions to remain, appearing as black regions in the core structure. The size and distribution of unreacted boron regions are similar in the filaments of wires annealed under different heat treatment conditions. This reveals that short-term low-temperature (650  $^{\circ}\text{C}$  - 15 min) annealing is sufficient for MgB2 phase formation.

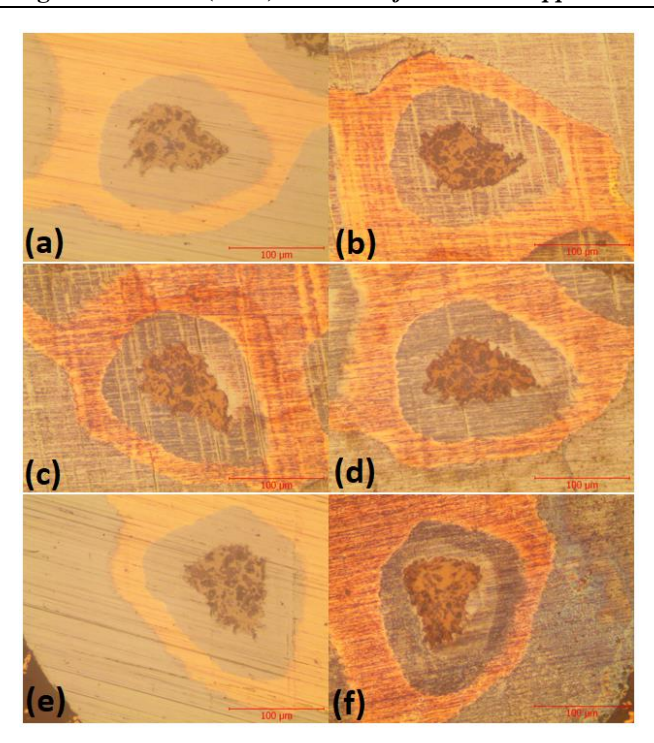


**Figure 6.** Single filament images taken with an optical microscope at 20x magnification from the cross-section of multifilament wires with a diameter of 0.82 mm. The multifilament wires are heat treated at different conditions, (a) 650 °C -15 min., (b) 650 °C -30 min, (c) 650 °C - 45 min., (d) 650 °C - 60 min., (e) 650 °C - 240 min., and (f) 700 °C - 60 min.

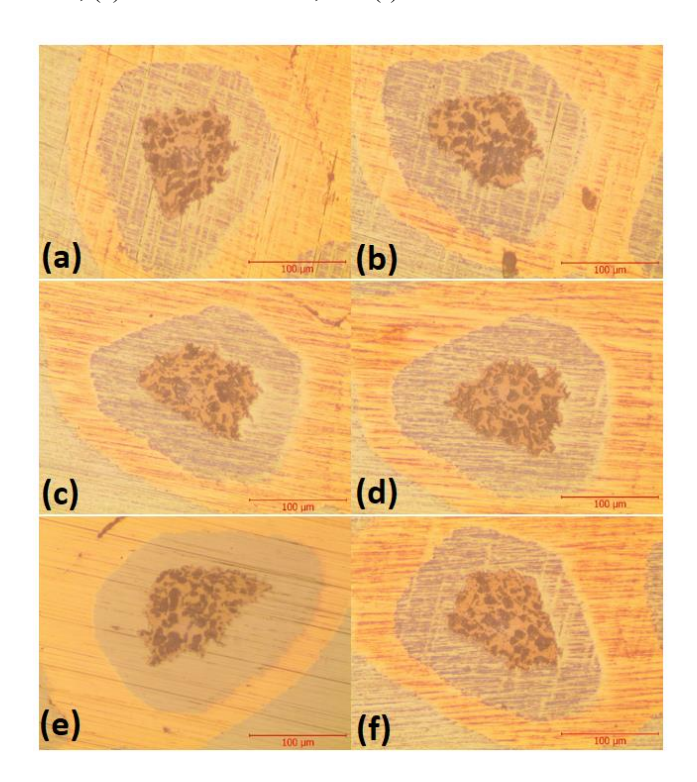


**Figure 7.** Single filament images taken with an optical microscope at 20x magnification from the cross-section of multifilament wires with a diameter of 1.02 mm. The multifilament wires are heat treated at different conditions, (a) 650 °C -15 min., (b) 650 °C -30 min, (c) 650 °C - 45 min., (d) 650 °C - 60 min., (e) 650 °C - 240 min., and (f) 700 °C - 60 min.

Figure 8 shows the Nb filaments obtained after etching the Fe and Cu sheath parts of the unreacted multifilament wire. An effective acidic solution was used in the etching process that selectively dissolved iron and copper without damaging the Nb

filaments (Chmielewski et al., 1997; Heini et al., 2017). The etching process was applied to wires with diameters of 1.50 mm, 1.02 mm, and 0.82 mm. Each wire was 6 cm in-length and the wire ends were securely sealed to avoid any reaction

between the MgB<sub>2</sub> core and acidic solution. After dissolving Fe and Cu layers, Nb filaments were successfully extracted as shown in Figure 8. Structural examination of these filaments was carried out using an optical microscope, and the images of Nb filaments are given in Figure 9. It is revealed that the sausage effect initiates at a diameter of 1.50 mm, as shown in the up row of Figure 9. A continuous cold drawing process from 1.50 mm to 0.82 mm diameter gradually increases the sausage effect and results in significant tear-ups on the surface of the Nb sheath, as shown in Figure 9. Some filaments exhibit notable deformations, such as cracks, sausage structures, and

tears (see Figure 10) but the many filaments for each diameter remain unaffected. These deformations arise due to non-uniformity in powder density within the wire (Shan et al., 2012). Furthermore, the agglomeration of B powder with large Mg particles can create non-uniform powder regions along the wire, making such deformations worse. In multifilament wires, filament deformations cannot be precisely detected from the outside; existing deformations in the filaments affect the flow of current throughout the entire wire and lead to adverse thermal instabilities which cause quench effects (Goldacker et al., 2004b).

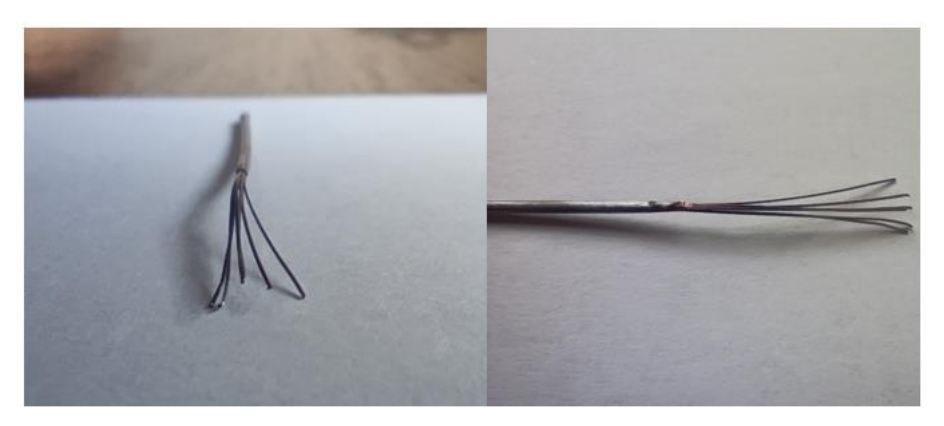
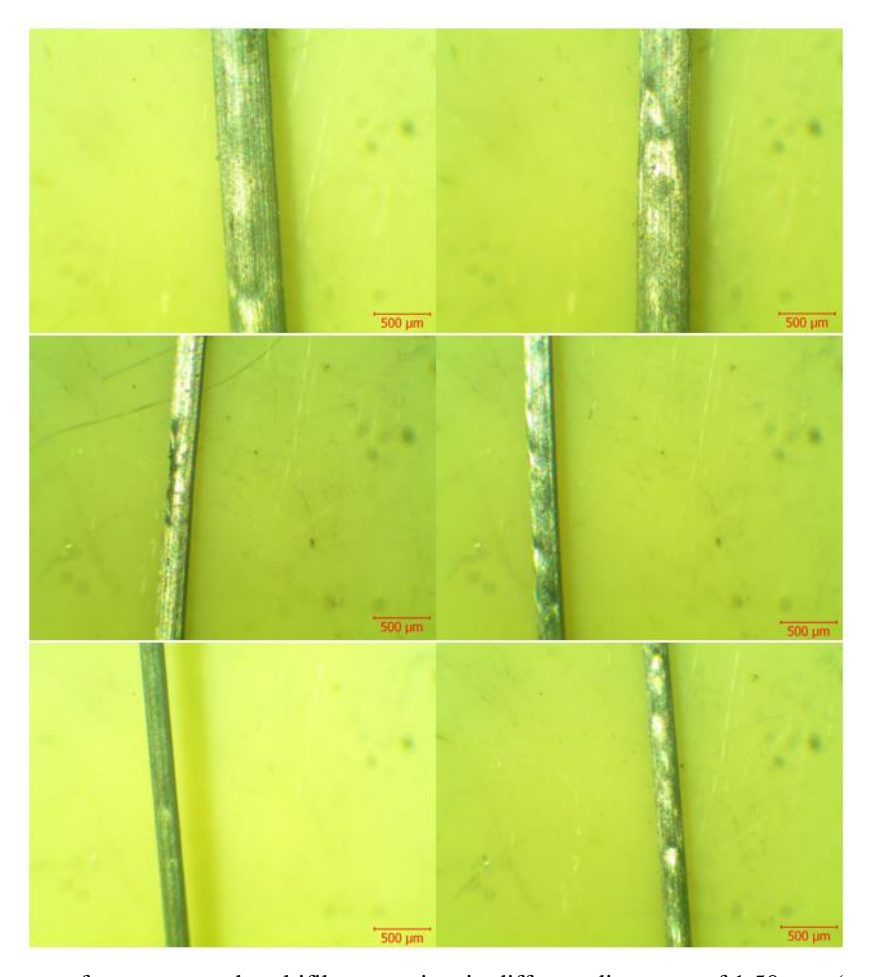
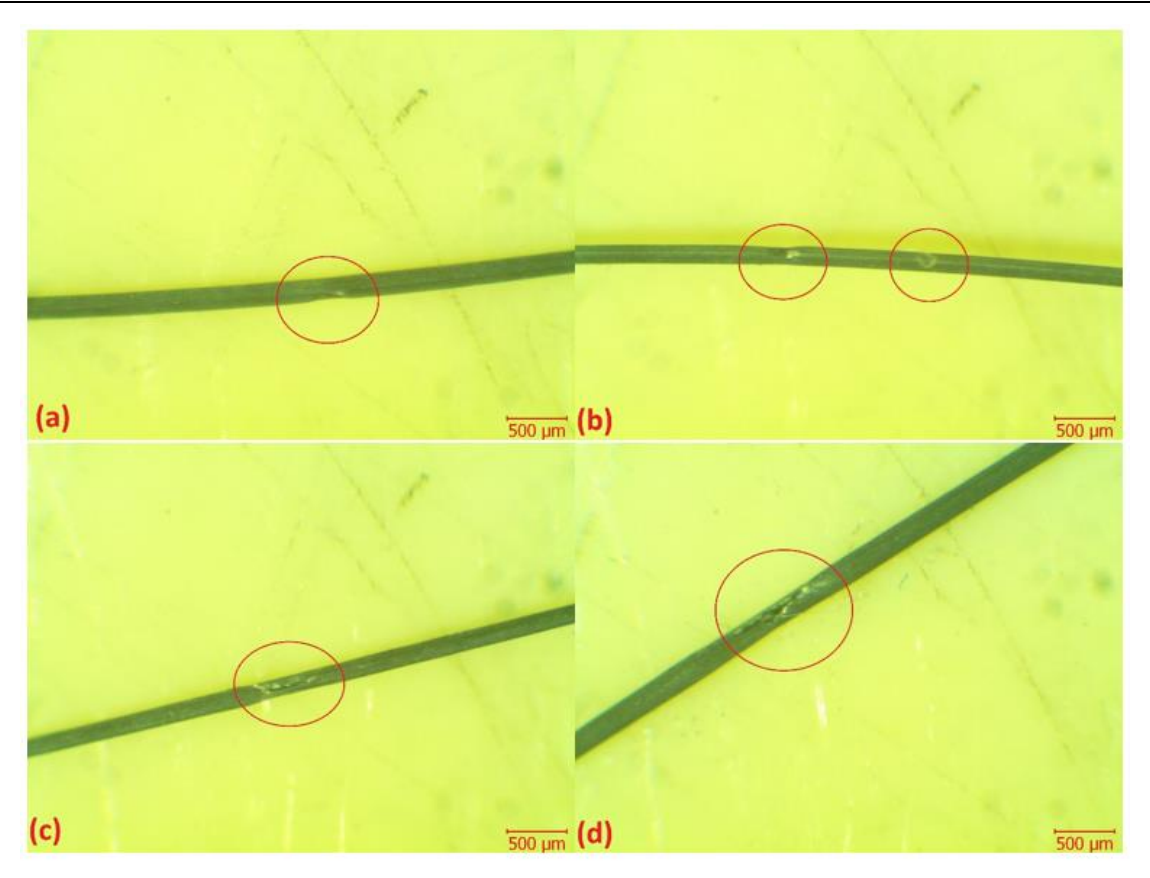


Figure 8. Nb/MgB<sub>2</sub> filaments of unreacted multifilament wire after etching process.



**Figure 9.** Nb mono filaments cut from unreacted multifilament wires in different diameters of 1.50 mm (top), 1.02 mm (middle), 0.82 mm (bottom).



**Figure 100.** Deformities on Nb filaments. The wire pieces were prepared using (a) - (b) 200-325 mesh Mg powder. (c) - (d) 100-200 mesh Mg powder.

#### 4. Conclusion

In this study, we examined possible structural problems on the inner surface of multifilament Fe/Cu/Nb/MgB2 wire produced by cold forming methods. It is observed that defects such as tearing and sausaging do not occur all along the wire, but they may occur at several arbitrary locations on some filaments. The production-related deformations worsen the transport properties of the wire as the wire diameter decreases. Our results suggest that the sausaging at large diameters may be a significant contributor to the tearing of the sheath material at small wire diameters. It is revealed that the superconducting core structures of the wires subjected to different thermal treatments are similar, so, a short-term low-temperature (650 °C - 15 min) annealing is sufficient for MgB<sub>2</sub> phase formation. Defects occurring in Nb/MgB2 filaments cannot be determined from the external structure of multifilament wires, but they negatively affect the transport properties of the wire. The use of finer Mg powder for initial Mg+2B mixture will benefit against filament deterioration (Fig. 10). The etching has emerged as an effective technique to study the structural properties of internal Nb filaments without damaging them. This is also important for joining MgB2 multifilament wires. As a result, we showed that Fe/Cu/Nb/MgB2 wires up to 0.82 mm in diameter can be produced without any major structural problems by cold forming method without applying strain-relief heat treatment.

#### Acknowledgment

This study was supported under titled "Bitter Type New Generation MgB2 Superconducting Solenoid Coil Construction and Characterisation" by the TUBİTAK, Grant No: 219M270.

#### **Conflict of Interest**

The authors declare that they have no conflict of interest.

#### References

Chmielewski, A. G., Urbtiski, T. S., & Migdal, W. (1997). Separation technologies for metals recovery from industrial wastes. *Hydrometallurgy*, 45(3), 333-344. https://doi.org/10.1016/S0304-386X(96)00090-4

Feng, Y., Yan, G., Zhao, Y., Liu, C. F., Fu, B.Q., Zhou, L., Cao, L. Z., Ruan, K. Q., Li, X. G., Shi, L., & Zhang Y. H. (2003). Superconducting properties of MgB<sub>2</sub> wires and tapes with different metal sheaths. *Physica C: Superconductivity*, 386, 598-602. <a href="https://doi.org/10.1016/S0921-4534(02)02169-X">https://doi.org/10.1016/S0921-4534(02)02169-X</a>

Goldacker, E., Schlachter, S. I., Obst B., & Eisterer, M. (2004a). *In situ* MgB<sub>2</sub> round wires with improved properties. *Superconductor Science and Technology*, 17, S490-S495. <a href="https://doi.org/10.1088/0953-2048/17/9/006">https://doi.org/10.1088/0953-2048/17/9/006</a>

- Goldacker, W., Sonja, I., Bing Liu, S., Obst, B., & Klimenko, E. (2004b). Considerations on critical currents and stability of MgB<sub>2</sub> wires made by different preparation routes. *Physica C: Superconductivity*, 401(1-4), 80-86. <a href="https://doi.org/10.1016/j.physc.2003.09.014">https://doi.org/10.1016/j.physc.2003.09.014</a>
- Heini, E., Sipi, S., Tero, J., Tuomas, S., Benjamin, P. W., Jari, A., & Mari, L. (2017). The effect of the redox potential of aqua regia and temperature on the Au, Cu, and Fe dissolution from WPCBs. *Recycling*, 2(3), 14. <a href="https://doi.org/10.3390/recycling2030014">https://doi.org/10.3390/recycling2030014</a>
- Jiawen, X., Xiaoze, P., Jie, S., Hideki, T., Yota, I., Min, Z., & Weijia, Y. (2019). Experimental test and analysis of AC losses in multifilamentary MgB<sub>2</sub> wire. *IEEE Transactions on Applied Superconductivity*, 29(5), 8201205. https://doi.org/10.1109/TASC.2019.2903924
- Koblischka, M. R., Alexander, W., Miryala, M., Inoue, K., Thomas, H., Bruno, D., Kevin, B., Masato, M., & Uwe, H. (2014). Development of MgB<sub>2</sub>-based bulk supermagnets. *IEEE Transactions on Magnetics*, 50(11), 9000504. <a href="https://doi.org/10.1109/TMAG.2014.2323995">https://doi.org/10.1109/TMAG.2014.2323995</a>
- Masayoshi, I., & Yuichi, O. (2023). Filament structure analysis of multifilament MgB<sub>2</sub> wires by using X-ray CT. *IEEE Transactions on Applied Superconductivity*, 33(5), 6200104. <a href="https://doi.org/10.1109/TASC.2023.3248540">https://doi.org/10.1109/TASC.2023.3248540</a>
- Nakane, T., Fujii, H., Matsumoto, A., Kitaguchi, H., & Kumakura, H. (2005). The improvement of in-situ powder in tube MgB<sub>2</sub> tapes by mixing MgB<sub>2</sub> to the starting powder of MgH<sub>2</sub> and B. *Physica C: Superconductivity and its Applications*, 426-431(Part 2), 1238-1243. https://doi.org/10.1016/j.physc.2005.02.147
- Patel, D., Al Hossain, M. S., Motaman, A., Barua, S., Shahabuddin, M., & Kim, J. H. (2014). Rational design of MgB<sub>2</sub>

- conductors toward practical applications. *Cryogenics*, *63*, 160-165. <a href="https://doi.org/10.1016/j.cryogenics.2014.04.016">https://doi.org/10.1016/j.cryogenics.2014.04.016</a>
- Shan, D., Yan, G., Zhou, L., Li, J. S., Li, C. S., Wang, Q. Y., Xiong, X. M., & Jiao, G. F. (2012). Multifilamentary MgB<sub>2</sub> wires fracture behavior during the drawing process. *Physica C: Superconductivity*, 483, 17-20. <a href="https://doi.org/10.1016/j.physc.2012.06.007">https://doi.org/10.1016/j.physc.2012.06.007</a>
- Suo, H. -L., Ma, L., Jiang, J. -M., Li, Y. -M., Zhang, Z. -L., Liu, M., Zhao, Y., He, D. -Y., & Zhou, M. -L. (2007). High Critical Current Densities in SiC Doped *In-Situ* MgB<sub>2</sub> wires prepared by continuous tube forming and filling technique. *IEEE Transactions on Applied Superconductivity*, 17(2), 2822-2825. https://doi.org/10.1109/tasc.2007.897457
- Tomsic, M., Rindflesich, M., Yue, J., McFadden, K., Phillip, J., Sumption, M. D., Bhatia, M., Bohnenstiehl, S., & Collings, E. W. (2007). Overview of MgB<sub>2</sub> superconductor applications. *International Journal of Applied Ceramic Technology*, 4(3), 250-259. https://doi.org/10.1088/0953-2048/18/5/026
- Vinod, K., Abhilash Kumar, R. G., & Syamaprasad, U. (2007).

  Prospects for MgB<sub>2</sub> superconductors for magnet application. Superconductor Science and Technology, 20(1), R1-R13. <a href="https://doi.org/10.1088/0953-2048/20/1/R01">https://doi.org/10.1088/0953-2048/20/1/R01</a>
- Xi, X. X. (2009). MgB<sub>2</sub> thin films. *Superconductor Science and Technology*, 22(4), 043001. <a href="https://doi.org/10.1088/0953-2048/22/4/043001">https://doi.org/10.1088/0953-2048/22/4/043001</a>
- Yao, W., Bascuñán, J., Hahn, S., & Iwasa, Y. (2010). MgB<sub>2</sub> coils for MRI applications. *IEEE Transactions on Applied Superconductivity*, 20(3), 756-759. https://doi.org/10.1109%2FTASC.2010.2044035



e-ISSN: 2979-9759



#### RESEARCH ARTICLE

# The Design and the Application of Off-Grid Solar Power System for a House in Kastamonu

Selcuk Emiralioglu • Secil Karatay • Faruk Erken •

Kastamonu University, Faculty of Engineering and Architecture, Department of Electrical-Electronics Engineering, Kastamonu/Türkiye

#### ARTICLE INFO

#### **Article History**

Received: 11.04.2024 Accepted: 06.05.2024 First Published: 22.06.2024

#### **Keywords**

Off-grid PV system Power plant Renewable energy Solar system



#### **ABSTRACT**

Off-grid solar power systems are becoming a more and more practical option for residential buildings looking to be environmentally friendly and achieve energy independence. This research offers a summary of an off-grid solar power system design specifically for a Kastamonu residential home. The study investigates the significance of using solar energy for a sustainable and dependable source of electricity, with an emphasis on the particular geographic and meteorological circumstances of the province. A system for creating off-grid solar energy systems is designed in this study with consideration for the weather and solar radiation in order to suit the unique energy requirements of a house in Kastamonu. It has been observed that 37.7% of the annual consumption of the selected house can be covered by the designed system and the system can amortize itself in 7.8 years. In general, residential off-grid solar power system design signifies a revolutionary turn towards sustainable energy methods, enabling homeowners to welcome a greener, more self-sufficient energy future.

#### Please cite this paper as follows:

Emiralioglu, S., Karatay, S., & Erken, F. (2024). The design and the application of off-grid solar power system for a house in Kastamonu. *Journal of Advanced Applied Sciences*, 3(1), 23-31. https://doi.org/10.61326/jaasci.v3i1.253

#### 1. Introduction

The concept of energy was initially proposed in the 17<sup>th</sup> century, and as scientists worked to understand life's mysteries, they advanced their research on it. A few centuries later, energy was first defined, enabling quantitative expression in already-existing physical systems. Numerous physical theories that derive from the principles of thermodynamics uphold the principle of energy conservation. Energy can therefore cause its own change and transformation, but it cannot be formed from nothing, nor can it destroy things that already exist. There are various types of energy, such as chemical, thermal, kinetic, potential, electrical, mechanical, magnetic, nuclear, sound, and light energy. Today, technology is allowing the energy that

drives technological advancement to continue developing on its own. Its energy has grown to such an extent that it is regarded as one of the most significant future building blocks. In the past, balancing production against consumption -which is currently the world's most pressing need- and even maintaining it at even higher levels, as well as the future discovery and development of a new world, were significant scientific concerns. Since their origin over millions of years ago, fossil fuels like coal, oil, natural gas, and nuclear power have been used for centuries to meet the energy needs of many regions worldwide, particularly in the domains of heat, electricity, and fuel. However, while it fosters economic leadership in areas with abundant resource reserves, it leaves these regions dependent on nations without

E-mail address: skaratay@kastamonu.edu.tr



<sup>&</sup>lt;sup>™</sup> Correspondence

reserves that are unable to supply their energy needs. Resources for energy appear to be more and more needed annually.

Energy has an impact on industry, communication, technology, the global economy, and political relations due to its necessity. The lack of sufficient production notwithstanding consumption and the impacts of fossil fuel usage on global warming are projected to generate energy crises in the future, prompting a quest for alternative energy sources. The most important criterion in energy production is that the resources are inexhaustible, reusable, recyclable and not as harmful to the environment as fossil fuels. There is a growing recognition that renewable energy sources, including geothermal, hydroelectric, solar, and wind power, are essential in meeting the pressing demand for sustainable energy generation. The shift to renewable energy is now essential due to the impending challenges of climate change, depleting fossil fuel supplies, and environmental damage. Numerous advantages come with renewable energy technologies, such as decreased air pollution, reduced greenhouse gas emissions, improved energy security, and stimulation of economic growth through the creation of jobs and new technology advancements. Furthermore, the decentralized energy system provided by renewables enables people and communities to produce their own electricity and contribute to a more egalitarian and resilient energy environment. Adopting renewable energy sources is socially and economically just as well as environmentally responsible, given the rising worldwide demand for energy (IPCC, 2024; IRENA, 2024; UNEP, 2024).

Solar power systems for houses have been a game-changer in the fight for sustainable energy. Through the installation of solar panels on roofs, homeowners can efficiently produce clean electricity to power their homes. Solar power systems benefit the environment by lowering carbon emissions and lowering reliance on fossil fuels, but they also improve the economy by lowering electricity costs and possibly earning money from selling extra energy back to the grid. Additionally, advancements in solar technology and declining installation costs have increased the availability of solar electricity for homeowners worldwide. A dependable and affordable investment for residential properties, solar panels also have a long lifespan and require little maintenance. Solar power systems are quickly becoming a necessary part of sustainable living for homes because of their ability to increase energy independence and contribute to a cleaner future (Solangi et al., 2011; Sahoo, 2016). Simple and dependable, solar power offers a steady, limitless supply of electricity without emitting any greenhouse gases. This is what makes it so beautiful. Solar panels give homes a practical means of lowering electricity bills in addition to lowering carbon footprints, offering long-term financial benefits as energy costs rise. Furthermore, solar installations are now more reasonably priced and within the reach of homes with different budgets because to technological advancements and economies of scale. Solar power systems not

only offer energy independence but also the opportunity for homeowners to become energy producers, adding to a more robust and decentralized energy infrastructure. An additional benefit of net metering is the ability to sell excess electricity back to the grid. Essentially, solar power systems for houses represent the perfect union of sustainability and usability, enabling people to take charge of their energy usage and fostering a cleaner, brighter future for future generations (Panwara et al., 2011; Bathaei & Streimikiene, 2023).

In recent years, the demand for home solar power systems has increased due to the increasing energy demand and the high cost of supplying energy. For this purpose, solar power system in residential area studies are intensively carried out in the literature (Faiers & Neame, 2006; Chehri & Mouftah, 2013; Wermager & Baur, 2013; El-Shahat et al., 2019). In Karaca and Dincer (2020), an integrated solar-based nature-friendly multigeneration power system containing a heat pump, an absorption chiller, photovoltaic-thermal panels, photo-electrochemical reactors, and a proton exchange membrane fuel cell to provide the useful outputs of heating, cooling, electricity, hot water, hydrogen production, and domestic wastewater treatment has been designed for residential houses. Energy and exergy methodologies along with thermodynamic analysis have been used to assess the system's overall performance. This study's findings have indicated that the suggested system can attain energy and energy efficiencies of 40% and 71.8%, respectively. In Tabassum et al. (2020), a small-scale Photo Voltaic (PV) based system has been designed within a housing compound or on the rooftop to generate sufficient power to support a household daily electricity usage. It has been observed that installing the solar PV system in the residential area has been viable in this study. In Shahabad et al. (2022), a model has been developed to assess the impact of subsidies after a thorough investigation into the relationship between the several elements influencing Iran's energy system's sustainability and the consequences of developing these power plants on it. The findings of this study have demonstrated that the technical aspect of the energy system's sustainability is positively impacted by the use of subsidies for the development of hybrid solar power plants (HSPPs) through distributed generation.

Makkiabadi et al. (2021) examine the quantity of electricity generated in Iran from solar energy. An economic and technical analysis is also conducted about the development of a 10 MW power plant in the city of Sirjan. The findings in this study indicate that a solar power plant in the Sirjan region may be constructed for US\$16.14 million, with a four-year payback period for the original investment. According to the data produced by the Homer software, July has the highest possible power generation. In Hamad et al. (2024), geospatial and techno-economic aspects with validated meteorological, social, and environmental parameters are blended in order to assess the potential and viability of solar power plants in Afghanistan. It has been noted that the most ideal locations are those that are

close to the transmission lines, where there is low water stress in addition to abundant solar resources and reasonably cool temperatures in this study. The poly-si REC module with the dual-axis tracking system is determined to have the largest yearly energy generation potential (166336 MWh/year), whereas the same module with the single-axis tracking system is projected to have the lowest levelized cost of electricity (0.031 \$/kWh). Kowsar et al. (2023) focus on a technoeconomic and environmental assessment utilizing PVsyst simulation tools for a 50 MW FSPV power plant for a marsh area in a very densely populated country. According to the study's findings, the 50 MW FSPV plant's levelized cost of energy (LCOE) is US\$ 0.051/kWh, which is somewhat less than the US\$ 0.087/kWh of fossil fuel-based power plants in the case study country.

In this study, it is investigated how outdoor lighting in landscape applications can be included as a design element in providing energy in solar energy systems and what should be taken into account in the design dimension, as well as how it can be used more efficiently within the framework of saving and renewal opportunities. The main purpose of the research is to evaluate the use of solar energy in lighting the house and its interaction with the landscape. The research also aims to use energy more efficiently and reduce fossil fuel consumption.

#### 1.1. Solar Energy Capacity in Kastamonu

Although the use of renewable energy sources increases every year, it takes time to renew and transform energy production systems based on fossil resources. The total global renewable energy capacity as of the end of 2018 is shown in Figure 1, within the data provided by the International Renewable Energy Agency (IRENA, 2024). When the data in Figure 1 is investigated, it is observed that there has been a significant increase in solar energy investments and installations among renewable energy sources in the last 10 years.

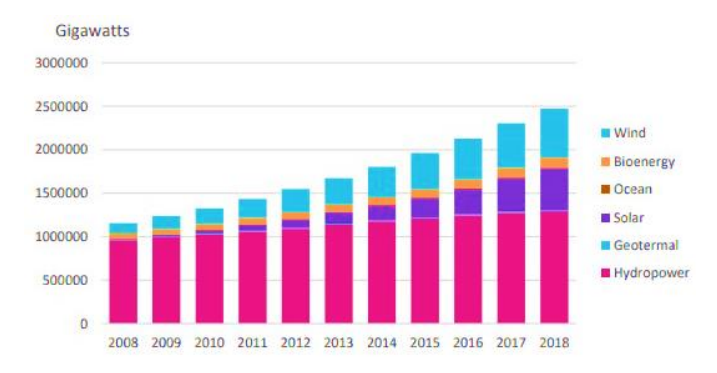


**Figure 1.** Renewable energy capacity in the world between 2008-2018.

Türkiye is located in a region called the sun belt, which is rich in solar energy. Türkiye, which has a high solar energy potential due to its geographical location, has an average annual total sunshine duration of 2.640 hours (total of 7.2 hours per day) and an average total radiation intensity of 1.311 kWh/m²-year (total of 3.6 kWh/m² per day). The solar energy potential is 380 billion kWh/year (EİGM, 2024). In 2023, 679 solar power plants are actively operating, providing a total installed power of 8.335 MW (Enerji Atlası, 2024). In Figure 2, the Total Solar Radiation is shown for all of Türkiye (EİGM, 2024).

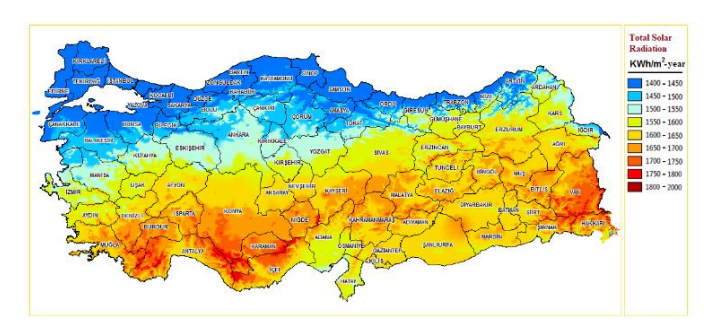
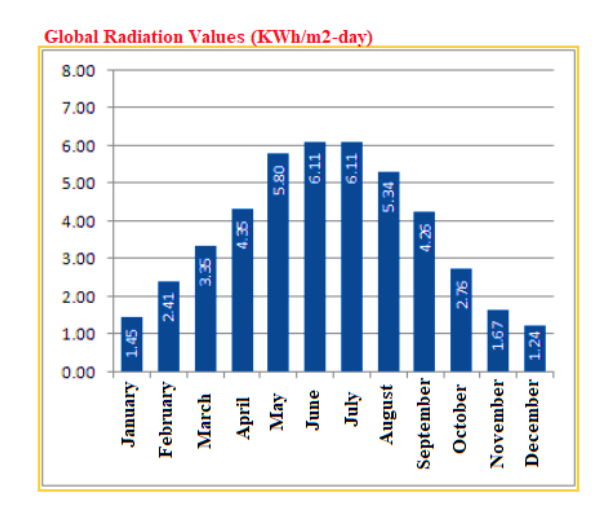


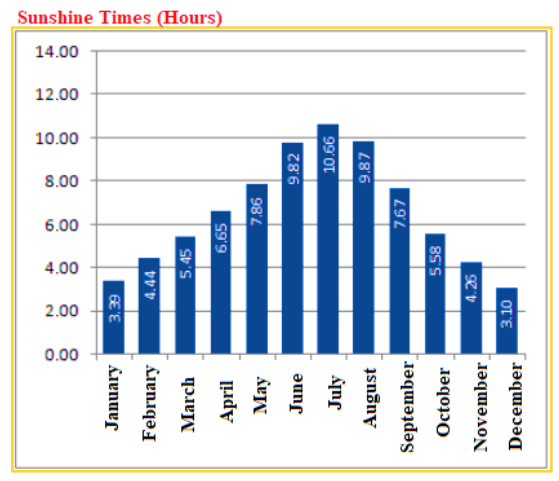
Figure 2. Solar energy potential atlas for Türkiye.

Kastamonu located in the Western Black Sea part of the Black Sea Region has a surface area of 13.108,1 km². Total energy consumption in Kastamonu with a population of 372.633, is 778.497 MWh. With this rate, the province has a rate of 0.39% in energy consumption in Türkiye. While the installed power (production) of power plants in the province is 41 MW, the installed power share in energy in Türkiye is 0.06%. The only source of energy production in the province is hydroelectric power plants (Arslan, 2016). In Figure 3, total solar radiation is given for Kastamonu. Figure 4 shows global radiation values in KWh/m²-day, sunshine times in hours and PV type-area-produced energy in kWh-year for Kastamonu.



**Figure 3.** Solar energy potential atlas for Kastamonu (EİGM, 2024).





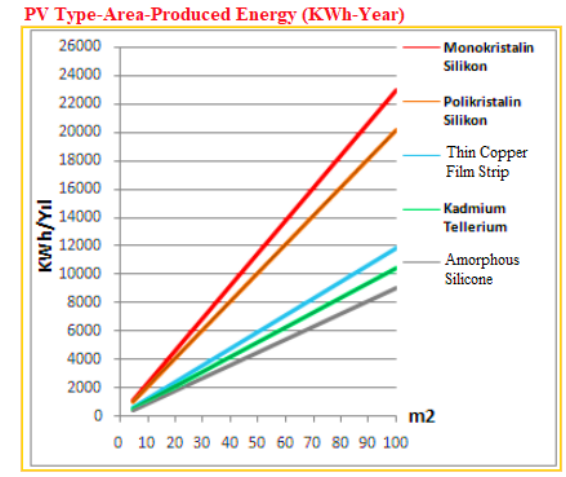


Figure 4. Global radiation values, sunshine times and PV type-area-produced energy (EİGM, 2024).

When it comes to total sun radiation, the Black Sea region, which includes Kastamonu, is one of the less promising areas. When Figure 3 is investigated, it is observed that the annual total solar radiation in no region within the borders of Kastamonu is more than 1650 kWh/m². The annual solar radiation rate throughout the province is mostly at the level of 1400-1450 kWh/m². This situation shows that the potential for solar energy production in Kastamonu is quite low on a provincial basis.

#### 2. Materials and Methods

#### 2.1. The Design

The main purpose of this study is to evaluate the use of solar energy and its interaction with the landscape in the lighting of a house in Kastamonu. The research also aims to use solar energy more efficiently and reduce fossil fuel consumption. In developing the proposed method for interior lighting of the house and evaluating the general features of the area has been formed with the "Protected Area Planning and Management" published in September 2007 by the General Directorate of Nature Conservation and National Parks under the Republic of Türkiye Ministry of Environment Urbanization and Climate

Change. The PV panels to be used have been placed at a 45-degree angle around the southwestern perimeter of a building in Kastamonu.

Systems independent of the grid are called off-grid systems. It is preferred in places where there is a network. In this case, the system also uses it connected to the network. Its most important feature is that it provides power supply via the grid line when needed in environments where electricity is not produced in sufficient quantity. However, when it is not fed back to the grid, it is considered an off-grid system (Boztepe, 2017). Such use would not be efficient or economical. Figure 5 shows the operation diagram of an off-grid system. These panels use photovoltaic cells to absorb sunlight and transform it into power. Usually, they are installed in arrays on the ground or on rooftops. The voltage and current from the solar panels that go to the battery are controlled by the charge controller. It guarantees that the batteries are charged effectively and avoids overcharging. Batteries are used to store the energy produced by the solar panels for use at a later time, usually when sunshine is scarce (such as at night or in overcast conditions). Lead-acid and lithium-ion batteries are typical battery types seen in offgrid systems. An inverter is required to transform the DC (direct current) electricity generated by the solar panels and stored in the batteries into AC electricity as the majority of household appliances and gadgets run on AC (alternating current). These parts offer together an enduring and dependable electrical source for off-grid uses such distant houses, cottages, RVs, boats, and telecommunications systems.

# Solar Panel Charge Controller Battery

Figure 5. Off-grid system diagram.

The fact that the land chosen in this study is a flat area and there are no restrictive factors does not pose any obstacle to the use of the land. Inclined placement of the panel is also one of the factors that increases the amount of energy. The panel is positioned at a 45-degree angle on the southwestern facade of the building selected within the scope of the study. The panels are arranged according to the southwest facade and a total of 2 are placed. The PV generator output of the panel, PV system climate data, PV generator surface, slope and placement direction of the PV module are given in Table 1.

Table 1. Features of the panel used and its placement.

PV System Climate Data	Kastamonu, TUR	
PV Generator Output	(1991-2010) 0.91 kWp	
PV Generator Surface	$4.4 \text{ m}^2$	
<b>Number of PV Modules</b>	2	
<b>Number of Inverters</b>	1	
Slope	6°	
<b>Placement Direction</b>	18° South	
Cell Type	Half-Cut	
<b>Maximum Power</b>	455 W	
Maximum Voltage	42 V	
<b>Maximum Current</b>	10.83 A	
<b>Open Circuit Voltage</b>	50.4 V	
<b>Short Circuit Current</b>	11.43 A	
Maximum System Voltage	1500 VDC	
Weight	24.0 kg	
Dimension	2096x1039x35	
Open Circuit Voltage Short Circuit Current Maximum System Voltage Weight	50.4 V 11.43 A 1500 VDC 24.0 kg	

Crystalline silicon cells are commonly used in solar panels. More efficient monocrystalline cells are more expensive. Two panels with a capacity of 455 W connected in series are used in this study. The operating values of the panel used depending on temperature and radiation are shown in Figure 6. The physical properties of the panel used are also given in Figure 7.

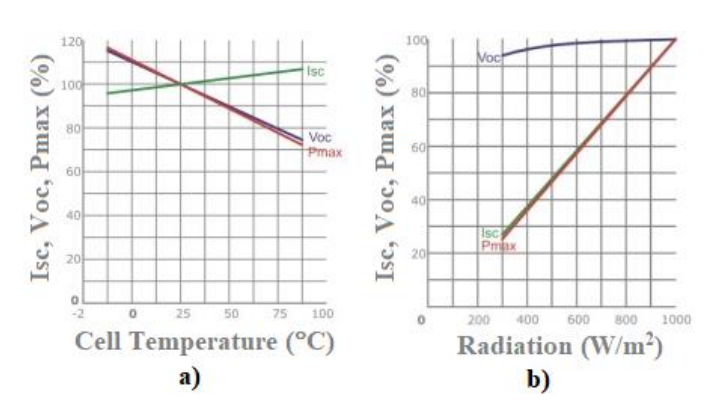


**Figure 6.** Variation of Isc, Voc and Pmax depending on a) temperature and b) radiation.

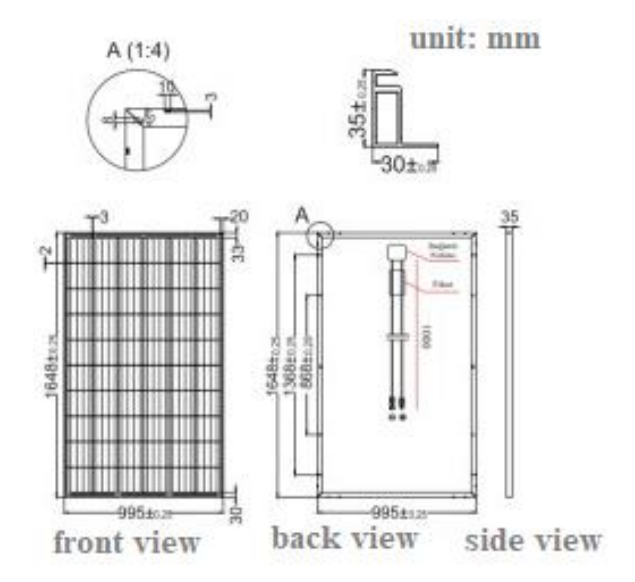


Figure 7. Physical properties of the used panel.

A converter with 10 kW DC-AC capacity is used in this study. The converter operates at a maximum efficiency of 82%. It has a maximum of 17 Amperes and 12-230 Volt adjustable output values. The technical specifications of the inverter used in the study are also given in Table 2.

**Table 2.** The technical specifications of the inverter used in the study.

stady.	
<b>Continuous Power</b>	1200 W
Instantaneous Power (30 ms)	2400 W
DC Input Voltage	12 V
AC Output Voltage	230 V
Efficiency	82%
<b>No-Load Current Consumption</b>	0.5 A
AC Output Waveform	Modified sine wave
<b>Operating Temperature</b>	0 °C - 40 °C
Low Voltage Battery Alarm Range	10 V - 10.4 V
Low Battery Voltage Shutdown Interval	9.7 V - 10 V
High Battery Voltage Shutdown Value	15 V
Weight	2.4 kg
Dimension	335x155x70 mm

While the solar charge controller or solar charge regulator prevents the battery and/or battery group from being damaged by overcharging or high voltage, it also serves to balance the voltage and current coming to the solar panel. The radiation values reaching the PV panel surface during the day cause different formation current and voltage values. The charge controller regulates the current coming from the panel and then ensures its transmission to the battery. It prevents the battery from overcharging and discharging according to its filling level by cutting off the current coming from the panels. The technical specifications of the solar control device used in the study are given in Table 3.

**Table 3.** The technical specifications of the solar control device used in the study.

Battery Voltage	12 V/24 V automatic	
<b>Charging Current</b>	50 A	
Discharge Current	50 A	
Equalization	B01 off 14.4 V	
B02 Jel	14.2 V	
B03 Sel	14.6 V	
Float Charge	13.7 V (default, adjustable)	
Discharge Stop	10.7 V (default, adjustable)	
<b>Discharge Reconnection</b>	12.6 V (default, adjustable)	
USB Output	5 V/3 A	
<b>Self-Consumption</b>	<10 mA	
<b>Operating Temperature</b>	-35 °C ~ +60 °C	
Weight	150 g	
Dimension	13.3x7x3.5 cm	

Data is monitored and recorded every 5 minutes for 24 hours. In the efficiency calculation, solar radiation per square meter should be taken into account first. Therefore, solar

radiation per square meter is calculated with the help of sensors located next to the panel group. This radiation is recorded by the system at 5-minute intervals. The energies entering the converter of the two panel series, which are formed by connecting two panels in series, are measured separately. After summing the energies of these two panel series, the efficiency of the panels is calculated as the ratio of the total solar energy falling on the panels as given below:

$$n_1 = \left(E_{input}/E_{solar}\right) x 100 \tag{1}$$

$$n_2 = (E_{output}/E_{input})x100 (2)$$

$$n_s = (E_{output}/E_{solar})x100 (3)$$

$$k_1 = ((E_{input} - E_{output})/E_{inpu})x100$$
 (4)

Here,  $n_1$ ,  $n_2$ ,  $n_s$  and  $k_1$  represent the energy loss in the efficiency in the panels, the inverter, the AC output and the converter sources, respectively.  $E_{solar}$  is the total solar energy coming to the panels (kWh),  $E_{output}$  is the AC electrical energy coming out of the converter (kWh) and  $E_{input}$  is the DC electrical energy entering the converter (kWh). The total energy produced by the system is also calculated with Equation 5:

$$E(hour) = powerx(5min/60min)$$
 (5)

The energy values in  $Watt \times minutes$  found after multiplying the power values obtained every 5 minutes by 5 minutes are divided by 60 minutes and the energy is calculated in  $Watt\ hours$ .  $E_{solar}$  is calculated by multiplying the solar energy per square meter by the panel surface area of 5 m<sup>2</sup>.

#### 3. Results and Discussion

The total daily consumption of the house selected within the scope of the study is 1590 W. The daily loss of the designed system is 2160 W. The minimum daily sunshine duration for Kastamonu is 2.4 hours. Therefore, the hourly installed power of the installed system is  $2160 \ W/2.4 \ h = 900 \ W = 0.9 \ kW$ . The required consumption amount is calculated monthly for the selected house. In Table 4, the energy consumption amounts of the house per device are given on a daily basis.

Figure 8 shows the annual values of total consumption for the pilot house, supplying the demand with the PV system and from the grid obtained using PV\*SOL (PV\*SOL, 2023). When Figure 8 is investigated, it is observed that while the annual consumption of the house is 1200 kWh, the amount supplied by the grid is 748 kWh and the amount supplied by the PV system is 452 kWh. This shows that 62.3% of the annual consumption can be supplied by the grid and 37.7% by the PV system. It is also observed that the autarky rate of the system is 37.7%. In Table 5, the average electricity consumption amount of the house and the average production amount of the power plant are given in W and Dollars. The calculation of production and consumption in Dollars is based on November 2023. When

Table 5 is examined, it is seen that the installed power of the system (hourly production) is 0.9 kW.

Table 4. Daily energy consumption values per device.

No	Device	Hourly Power (Watt)	Operating Time (hour)	Daily Energy Consumption
1	Lcd Tv	100 W	5	500 W
2	Lightbulb	12 W	5	60 W
3	Phone	5 W	4	20 W
4	Computer	15 W	4	60 W
5	Freezer	50 W	10	500 W
6	Deep freeze	40 W	10	400 W
7	Sconce	10 W	5	50 W

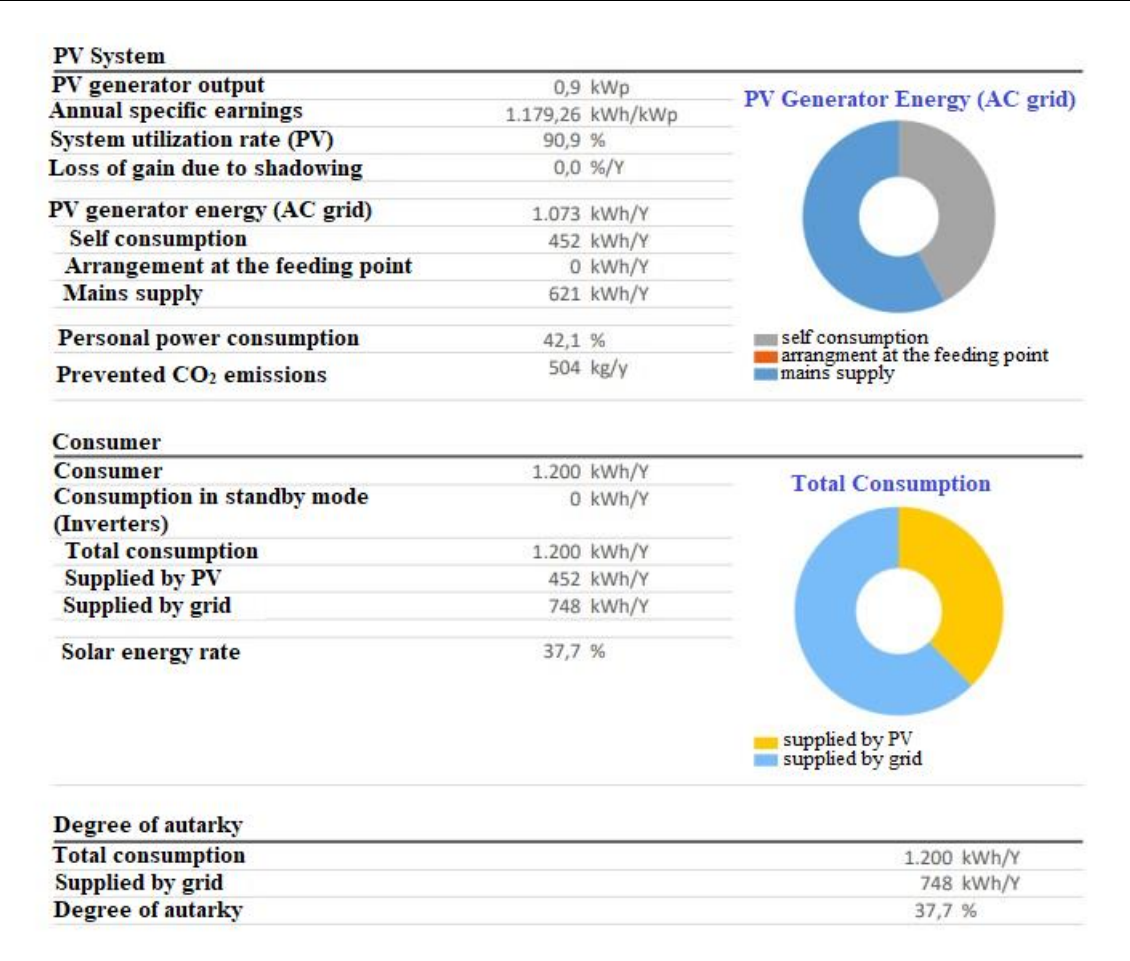


Figure 8. Annual values of consumption of the house and supplied by the grid and PV system.

**Table 5.** Average electricity consumption and production values of the house and the power plant in Dollars and W.

	Annual	Monthly	Daily	Hourly
Avorage Electricity Congumentian of the House	\$62.17	\$5.18	\$0.52	\$0.035
Average Electricity Consumption of the House	900W	100 W	10 W	0.4 kW
Avonage Electricity Duodystian Amount of the Dower Dlant	\$82.90	\$6.4	\$0.8	\$0.04
Average Electricity Production Amount of the Power Plant	1200 W	125 W	15 W	0.65  kW

The annual radiation value in Kastamonu is 1.384 kW/m<sup>2</sup>. The electricity sales price is \$0.133 per kW. The hourly lossy production power of the designed power plant is 6.55 kW. The installation cost of the power plant for 1 kW is \$600. According

to these data, Table 6 shows the financial analysis obtained using the PV\*SOL application. When Table 6 is investigated, it is observed that the grid supply in the first year is 621 kW per year and the PV generator output is 0.9 kWp. It is also observed

that the amortization period of the installed power plant is 7.8 years. With the installed power plant, an annual profit of 12.65% is obtained from the consumption cost. Annual yield is

also increasing every year. Table 7 gives the detailed cost calculation of the installed power plant.

Table 6. Financial analysis of the installed system obtained from PV\*SOL.

System Information				
Grid supply within two years (including module performance degradation)	621	kWh/Year		
PV generator output	0.9	kWp		
Commissioning of the system	30.12.2023			
Evaluation period	20	Years		
Interest applied to principal	1	%		
Economic Parameters				
Return on assets	12.65	%		
Accumulated cash flow (cash balance)	79,88	\$		
Amortization period	7.8	Years		
Electricity Generation cost	0.0024	\$		
Payments Overview				
Certain investment expenses	51,50	\$		
Investment costs	46,80	\$		
One-time payments	0,00	\$		
Incoming subsidies	0,00	\$		
Annual expenses	0,00	\$		
Other income or savings	0,00	\$		

**Table 7.** Detailed price display of materials.

	Piece	Price	Amount
Inverter	1	\$145	\$145
Panel	2	\$190	\$380
Battery	1	\$104	\$104
<b>Grand total</b>			\$629

A solar power system for a house in Kastamonu, where the sunshine duration is minimum 2.4 hours, is designed in this study. Two panels with a capacity of 455 W are used in the designed system. The inverter in the system operates with a maximum efficiency of 82%. Moreover, a solar controller is used to balance the voltage and current coming to the solar panels while preventing the system from being damaged by high voltage. The daily consumption of the pilot house is 10 W and the hourly loss production power of the designed power plant is 6.55 kW.

#### 4. Conclusion

In summary, designing and installing off-grid solar power systems for residential buildings is a critical first step toward long-term, sustainable energy independence. These systems give homeowners the chance to reduce their carbon impact and break free from traditional energy dependence through careful planning and integration of cutting-edge technologies. In addition to being a dependable supply of electricity in isolated

or underdeveloped locations, off-grid solar power systems also provide resilience against power outages and natural catastrophes. Homeowners can benefit from a continuous power source, reduced energy costs, and a better environment by utilizing the sun's plentiful energy. Furthermore, developments in off-grid solar technologies, like better energy management and battery storage systems, are raising the systems' price and efficiency. Off-grid solar power systems are predicted to become more popular as the need for renewable energy sources increases, spurring innovation and further bringing down costs.

In order to save energy and lower energy costs, an off-grid solar power system has been designed for a house in Kastamonu in this work. The total cost of the system, including the inverter, panel and battery, is \$629. The average annual energy consumption of the pilot house is 1200 kWh. It is observed that approximately 452 kWh of the house's 1200 kWh consumption can be supplied by the designed system. This shows that 37.7% of the total annual energy consumption will be met and saved by the designed system. It is concluded that the amortization period of the designed system according to the total cost is 7.8 years. Off-grid solar power essentially signifies a paradigm change in domestic energy usage, enabling homeowners to embrace sustainability and take charge of their own energy future. Off-grid solar power systems open the door to a more promising and sustainable future for both homes and the

environment with their thoughtful planning, creative design, and continuous support.

#### Acknowledgment

This study was carried out within the scope of Kastamonu University Electrical and Electronics Engineering Department EEM 401 Electrical and Electronics Engineering Design course.

#### **Conflict of Interest**

The authors declare that they have no conflict of interest.

#### References

- Arslan, F. (2016). *The renewable energy potential in Kastamonu*. 1<sup>st</sup> International Abana Symposium. Kastamonu.
- Bathaei, A., & Streimikiene, D. (2023). Renewable energy and sustainable agriculture: Review of indicators. *Sustainability*, *15*(9), 14307. <a href="https://doi.org/10.3390/su151914307">https://doi.org/10.3390/su151914307</a>
- Boztepe, M. (2017). Fotovoltaik güç sistemlerinde verimliliği etkileyen parametreler. *EMO İzmir Şubesi Aylık Bülteni*, 321, 13-17. (In Turkish)
- Chehri, A., & Mouftah, H. T. (2013). FEMAN: Fuzzy-based energy management system for green houses using hybrid grid solar power. *Journal of Renewable Energy*, 2013, 2-7. <a href="https://doi.org/10.1155/2013/785636">https://doi.org/10.1155/2013/785636</a>
- EİGM. (2024). Güneş enerjisi potansiyel atlası. Enerji İşleri Genel Müdürlüğü (EİGM). <a href="https://gepa.enerji.gov.tr/MyCalculator/">https://gepa.enerji.gov.tr/MyCalculator/</a> (In Turkish)
- El-Shahat, A., Haddad, R. J., Courson, J., Martenson, A., & Mosley, A. (2019). *Solar-powered house system design*. 2019 SoutheastCon. Huntsville.
- Enerji Atlası. (2024). *Güneş enerji santralleri*. Enerji Atlası. <a href="https://www.enerjiatlasi.com/gunes/">https://www.enerjiatlasi.com/gunes/</a> (In Turkish)
- Faiers, A., & Neame, C. (2006). Consumer attitudes towards domestic solar power systems. *Energy Policy*, *34*(14), 1797-1806. <a href="https://doi.org/10.1016/j.enpol.2005.01.001">https://doi.org/10.1016/j.enpol.2005.01.001</a>
- Hamad, J., Ahmad, M., & Zeeshan, M. (2024). Solar energy resource mapping, site suitability and techno-economic feasibility analysis for utility scale photovoltaic power plants in Afghanistan. *Energy Conversion and Management*, 303, 1-14. https://doi.org/10.1016/j.enconman.2024.118188
- IPCC. (2024). *Reports*. The Intergovernmental Panel on Climate Change (IPCC). <a href="https://www.ipcc.ch/">https://www.ipcc.ch/</a>

- IRENA. (2024). *International renewable energy agency*. The International Renewable Energy Agency (IRENA). <a href="https://www.irena.org/">https://www.irena.org/</a>
- Karaca, A. E., & Dincer, I. (2020). A new integrated solar energy based system for residential houses. *Energy Conversion and Management*, 221, 113112. <a href="https://doi.org/10.1016/j.enconman.2020.113112">https://doi.org/10.1016/j.enconman.2020.113112</a>
- Kowsar, A., Hassan, M., Rana, M. T., Haque, N., Faruque, M. H., Ahsan, S., & Alam, F. (2023). Optimization and techno-economic assessment of 50 MW floating solar power plant on Hakaluki marsh land in Bangladesh. *Renewable Energy*, 216, 119077. https://doi.org/10.1016/j.renene.2023.119077
- Makkiabadi, M., Hoseinzadeh, S., Taghavirashidizadeh, A., Soleimaninezhad, M., Kamyabi, M., Hajabdollahi, H., Nezhad, M. M., & Piras, G. (2021). Performance evaluation of solar power plants: A review and a case study. *Processes*, 9(12), 2253. <a href="https://doi.org/10.3390/pr9122253">https://doi.org/10.3390/pr9122253</a>
- Panwara, N. L., Kaushik, S. C., & Kothari, S. (2011). Role of renewable energy sources in environmental protection: A review. *Renewable and Sustainable Energy Reviews*, *15*(3), 1513-1524. https://doi.org/10.1016/j.rser.2010.11.037
- PV\*SOL. (2023). PV\*SOL. https://pvsol.software/en/
- Sahoo, S. K. (2016). Renewable and sustainable energy reviews solar photovoltaic energy progress in India: A review. *Renewable and Sustainable Energy Reviews*, 59, 927-939. https://doi.org/10.1016/j.rser.2016.01.049
- Shahabad, M. E., Mostafaeipour, A., Nasab, H. H., Sadegheih, A., & Xuan, H. A. (2022). A new model to investigate effects of subsidies for home solar power systems using system dynamics approach: A case study. *Sustainable Energy Technologies and Assessments*, 49, 101706. https://doi.org/10.1016/j.seta.2021.101706
- Solangi, K., Islam, M., Saidur, R., Rahim, N., & Fayaz, H. (2011). A review on global solar energy policy. *Renewable and Sustainable Energy Reviews*, 15(4), 2149-2163. https://doi.org/10.1016/j.rser.2011.01.007
- Tabassum, M., Kashem, S. B., & Ahmed, J. (2020). Feasibility study of solar power system in residential area. *International Journal of Innovation in Computational Science and Engineering*, *1*(1), 10-17.
- UNEP. (2024). *United nations environment programme*. The United Nations Environment Programme (UNEP). <a href="https://www.unep.org/">https://www.unep.org/</a>
- Wermager, S., & Baur, S. (2013). Energy analysis of a student-designed solar house. *Energies*, 6(12), 6373-6390. https://doi.org/10.3390/en6126373



e-ISSN: 2979-9759



#### RESEARCH ARTICLE

# Frequency Dependent Negative Dielectric Behavior in Parylene C Based Composite Films

Utku Guduloglu¹ • Sedat Kurnaz² • Turgay Seydioglu³ • Gizem Bekar⁴ • Ozgur Ozturk⁵ •

#### ARTICLE INFO

#### **Article History**

Received: 22.04.2024 Accepted: 04.06.2024 First Published: 22.06.2024

#### Keywords

Dielectric Negative capacitance Parylene C Polymer



#### ABSTRACT

Dielectric materials are an important research topic for many applications today. Polymers are among the prominent dielectrics due to their durability, high ionic conductivity and low dielectric losses. This study investigates the dielectric properties of Parylene C (PAC)-based composite films. Capacitance and dissipation factor values are measured. Dielectric permittivity and losses are calculated. Negative capacitance and negative dielectric constant are observed, and resonant frequency values are compared. Activated carbon doping significantly impacts the resonant frequencies of the films. Doped samples exhibit higher positive and negative resonant frequencies (2.2560 MHz and 2.2593 MHz) compared to undoped counterparts (2.1952 MHz and 2.2015 MHz). Polarization further increases resonant frequencies, alongside dielectric permittivity and dissipation factor with permittivity experiencing a more pronounced increase. Post-polarization, doped samples display resonant frequencies of 2.3727 MHz and 2.3761 MHz, while undoped samples reach 2.3658 MHz and 2.3727 MHz. A comprehensive analysis of impedance, resistance, and reactance values reveals insights into the composite film's behavior. Crucially, throughout the measurements, the composite films display a consistent inductive response at frequencies above their resonance frequencies. Understanding the mechanisms behind this inductive response could open up new possibilities for the use of these films in advanced electronic devices and circuits.

#### Please cite this paper as follows:

Guduloglu, U., Kurnaz, S., Seydioglu, T., Bekar, G., & Ozturk, O. (2024). Frequency dependent negative dielectric behavior in parylene C based composite films. *Journal of Advanced Applied Sciences*, *3*(1), 32-39. https://doi.org/10.61326/jaasci.v3i1.254

#### 1. Introduction

Negative capacitance effect in ferroelectric materials has attracted many researchers' attention recently (Wong & Salahuddin, 2018). The presence of negative capacitance in a material means that the material exhibits an inductive behaviour (Jones et al., 1998). The Landau-Ginzburg-Devonshire model,

which models the phenomena in ferroelectric materials, explains the emergence of the definition of negative capacitance. According to this model, in the energy barrier region between energy minima, where the polarisation value is close to 0 ( $P\approx0$ ), the ferroelectric has negative capacitance (Hoffmann et al., 2019). Another explanation for the negative

E-mail address: sedatkurnaz@kastamonu.edu.tr



<sup>&</sup>lt;sup>1</sup>Bartın University, Faculty of Engineering, Architecture and Design, Department of Electrical and Electronics Engineering, Bartın/Türkiye

<sup>&</sup>lt;sup>2</sup>Kastamonu University, Central Research Laboratory, Kastamonu/Türkiye

<sup>&</sup>lt;sup>3</sup>Kastamonu University, Vocational School, Department of Electronics and Automation, Kastamonu/Türkiye

<sup>&</sup>lt;sup>4</sup>Sinop University, Ayancık Vocational School, Department of Electronics and Automation, Sinop/Türkiye

<sup>&</sup>lt;sup>5</sup>Kastamonu University, Faculty of Engineering and Architecture, Department of Electrical and Electronics Engineering, Kastamonu/Türkiye

<sup>&</sup>lt;sup>™</sup> Correspondence

capacity is the reduction of the effective voltage across the capacitor during ferroelectric switching. Examples of potential applications of negative capacitance materials today include field-effect transistors, energy storage, high-power microwave filters (Hoffmann et al., 2019; Sun et al., 2019). Negative capacitance has been difficult to measure because the material does not exhibit stable behaviour in the negative capacitance state. However, since materials with negative capacitance behaviour show the characteristics of a series inductorcapacitor circuit, stabilisation can also be achieved in the negative capacitance state by using the series capacitor model (Khan et al., 2015; Z. Wang et al., 2020). In the series capacitor model, the total capacitance is equal to the series equivalent of the capacitance of each dielectric, and "dielectric resonance" occurs when the frequency takes on the value  $f=1/2\pi(LC)$ , thus clearly obtaining negative capacitance in the resonant frequency region. In the negative capacitance state, the capacitor spontaneously charges. This saves energy by enabling nanoelectronic applications with very low power consumption (Íñiguez et al., 2019).

The dielectric constant  $(\varepsilon_r)$  also known as relative permittivity, is a fundamental material property that quantifies the ability of a substance to store electrical energy within an electric field. It serves as a critical parameter in diverse fields such as materials science, chemistry, and physics. The dielectric constant significantly influences the polarization behavior, energy storage capacity, and overall electrical properties of materials. The real component of the dielectric constant is represented by dielectric permittivity ( $\varepsilon$ ), while the imaginary component is represented by dielectric loss ( $\varepsilon''$ ) (Xie et al., 2022). Materials exhibiting negative capacitance necessarily possess negative permittivity due to the relationship described by the equation:  $C = \varepsilon_0 \varepsilon_r A/d$  where  $\varepsilon_0$  is the vacuum permittivity,  $\varepsilon_r$  is the dielectric permittivity, A is the surface area of the sample and d is the thickness of the film. Negative permeability is a phenomenon typically observed at frequencies of megahertz (MHz) and above (Yan et al., 2013). The Drude and Lorentz models are instrumental in elucidating the behavior of negative permittivity, not negative permeability. The Drude model, a cornerstone in understanding the transport properties of electrons in metals, describes electron conduction in solids by considering induced electronic polarization. This is achieved by introducing an auxiliary particle, attached to each polarizable atom via a harmonic spring (Jiang et al., 2010). According to the Drude model, when the contribution of the conducting material surpasses a certain threshold, the structure becomes conductive, and the collective movement of electrons results in negative permittivity.

The Lorentz resonance model is a fundamental concept used to understand the behavior of resonant systems, particularly in the context of electromagnetic phenomena. This model finds widespread application in fields like optics, materials science, and physics to analyze and predict the response of resonant systems to external stimuli (Oughstun & Cartwright, 2003; Romano et al., 2014). According to the Lorentz model, when the doping concentration of a conducting material is below the percolation threshold, the conducting phase remains isolated, and induced dipoles form. These dipoles, through resonance, can cause the dielectric constant to decrease, potentially reaching negative values. However, it is important to note that both the Drude and Lorentz models have limitations in fully explaining the complexities of dielectric behavior (Leng et al., 2020). A negative dielectric constant signifies a situation where charges align in the opposite direction to the applied voltage. In recent years, there has been growing interest in metamaterials exhibiting this property. Potential applications of metamaterials with negative dielectric constants include sensors, antennas, wireless transmission systems, and capacitors (Qu et al., 2019; Balu et al., 2020; Liu et al., 2020).

Complex impedance spectroscopy is an important study commonly used for observe the dielectric properties of dielectric materials. Impedance is a complex parameter that indicates the resistance of a material to alternating current and can be expressed by the expression Z = R + jX or Z = Z' + jZ''. Here R is the resistance, which is the real part of the impedance, and X is the reactance, which is the imaginary part of the impedance (El-Nahass et al., 2014; Sankar et al., 2022). Impedance analyses has been used to characterize some materials including polymers and developed some electronic devices (Raja et al., 2004).

Polymer dielectrics are commonly used in various applications due to their lightweight nature, scalability, mechanical flexibility, high dielectric strength, and reliability. However, these materials face limitations, particularly in high temperature (exceeding 150 °C) and high energy storage applications. Furthermore, the dielectric constants of polymer materials are often limited and it is not meet the requirements for high energy storage dielectric capacitors (Dong et al., 2023). Also, the flashover issue at the interfaces of polymer dielectrics with other substances poses a significant challenge, as the breakdown voltages at these interfaces are lower than those for the dielectrics alone, affecting the safe and reliable operation of the materials (T. Wang et al., 2022). So, to remove these limitations, the development of polymer nanocomposites with rationally designed nanostructured inorganic fillers has shown promise in improving the capacitive performance of polymer materials (Li et al., 2019).

In this study, we investigate the dielectric properties of PAC-based composite films, focusing on the influence of activated carbon doping. The analysis encompasses the impact of doping on resonant frequency, negative capacitance regions, dielectric permittivity and losses, and complex impedance parameters. Furthermore, we examine the effects of the polarization process on the dielectric properties of the composite films.

#### 2. Materials and Methods

The synthesis process of PAC consists of three steps: sublimation, pyrolysis, and deposition. In the sublimation step, the granular dimer was vaporized at 150 °C. The dimeric gas was transferred to the pyrolysis furnace using argon gas and a vacuum pump. In the pyrolysis step, the dimeric gas was then split into a monomeric gas at a temperature of 650 °C. Finally, the monomeric gas was released into the coating chamber to be deposited on the glass substrate under a vacuum of 0.6 Pa at room temperature. To capture the excess PAC, a cold trap was placed in front of the pumping system. After deposition, the PAC films were removed from the glass substrate by using a tweezers and acetone. The synthesized PAC was dissolved in 50 ml of 1, 2 dichlorobenzene at 160 °C for 6 h with stirring. The PU, PMMA, and AC were added in different weight ratios to mix the solution homogeneously for 1 h at the same temperature. The solution was cooled by mixing, and 20 ml of acetone at 50 °C was added and stirred for 30 min. The samples were labelled as 0C and 1C based on the weight ratio of the ACs in the polymer matrix (Table 1) (Kurnaz et al., 2023).

**Table 1.** The mass ratio of polymer composites in the mixture.

Samples	PAC (%)	PU (%)	PMMA (%)	AC (%)
0C	50	45	5	0
1C	50	44	5	1

Capacitance measurements were carried out by an impedance analyzer (Wayne Kerr 6500B) at 1-10 MHz with a 1  $V_{\rm AC}$  signal at room temperature. At the same time, the dielectric properties were examined with an impedance analyser as a result of polarisation processes by applying 1 kV voltage for 10 minutes at 60 °C temperature.

#### 3. Results and Discussion

Figure 1a shows the frequency dependence of the capacitance value of the samples prior to polarisation. The graph clearly shows the resonance frequency value and the peaks that occur in this region. It can be seen that the activated carbon additive causes a shift in the resonance frequency region. For 0C, the positive resonant frequency is 2.1952 MHz and the negative resonant frequency is 2.2015 MHz. For the 1C, the positive and negative resonant frequencies are 2.2560 MHz and 2.2593 MHz respectively. The transition to negative capacitance is clearly seen at frequencies after the positive resonant frequency. This shows that the inductive behaviour dominates the capacitive behaviour from the positive resonant frequency of the film. The resonance frequencies of 1C are higher than those of OC. They are shifted towards higher frequencies. In the measurements made after polarisation, the resonant frequencies are slightly higher than before polarisation (Figure 1b). It can be seen that this also leads to an increase in the values of the capacitance. For the 0C, the positive resonant

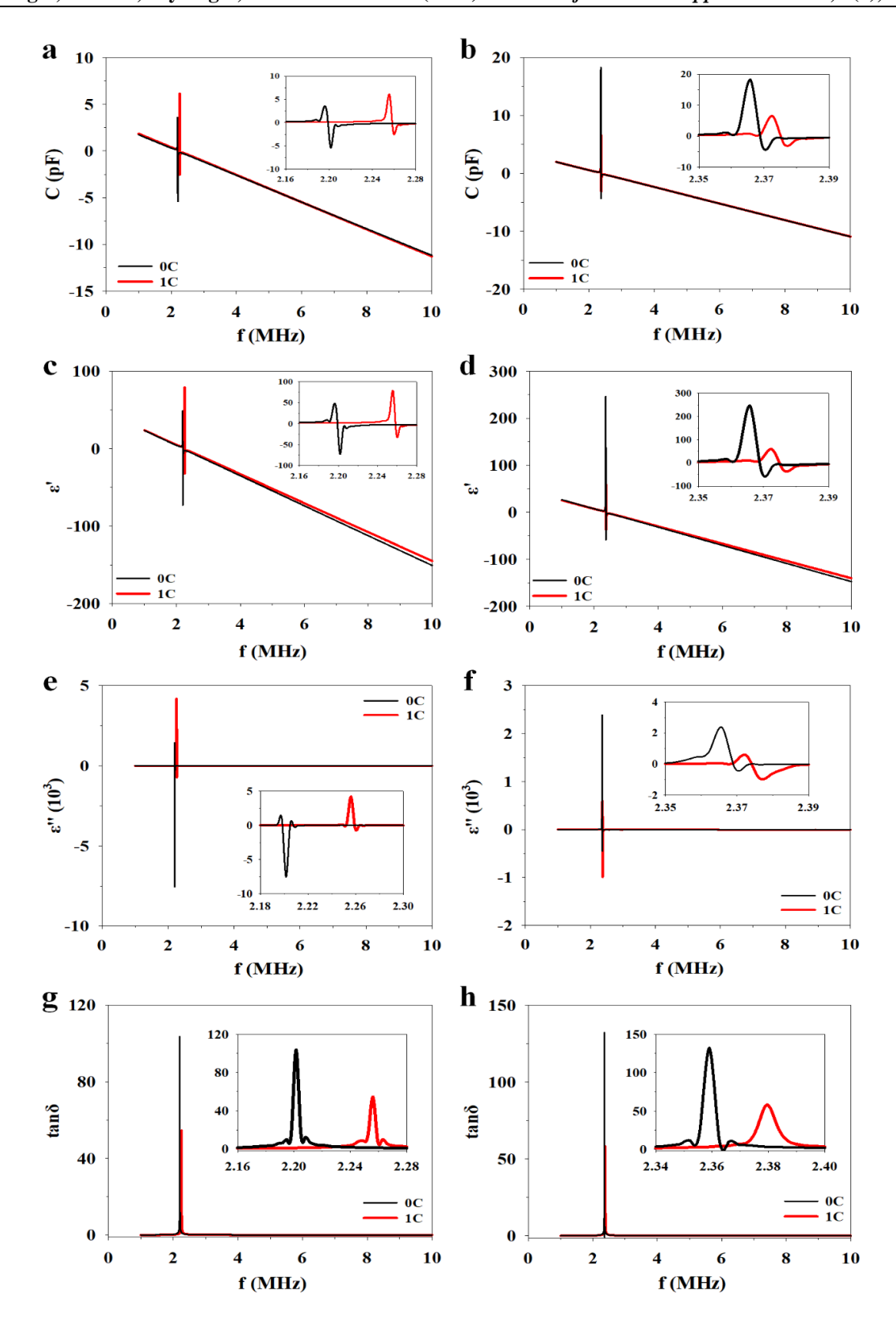
frequency is 2.3658 MHz and the negative resonant frequency is 2.3727 MHz. For 1C the positive and negative resonant frequencies are 2.3727 MHz and 2.3761 MHz respectively. Depending on the polarisation, the change at 1C is greater than 1.8 pF and the change at 0C is 11.91 pF. This is actually due to the decrease in the amount of PU in the film, which exhibits dielectric behaviour (Vandeparre et al., 2013; D. Wang et al., 2013). The frequency dependence of the permittivity of the samples before and after polarisation is shown in Figure 1c and 1d. The value of the dielectric constant is calculated from capacitance measurements. The permittivity is directly proportional to the capacitance and shows a similar behaviour to Figure 1a and 1b. The permittivity at the positive resonant frequency is 44.23 for the 0C and 77.01 for the 1C. It is -72.85 for 0C and -25.34 for 1C at the negative peak resonant frequency (Figure 1c).

After polarisation, the permittivity at the positive resonant frequency is 246.6 for 0C and 58.58 for 1C. At the negative peak resonant frequency, it is calculated to be -31.25 for 0C and -25.34 for 1C. It can be seen that polarisation reduces the negative permittivity values (Figure 1d). Mokni et al. (2019) measured the dielectric permittivity value of PAC to be approximately 5 at a frequency of 1 MHz. In other studies, results are obtained that show a low dielectric permittivity (Kahouli et al., 2009; Hu et al., 2022). In this study, it is quite high in the PAC-based composite film. At a frequency of 1 MHz, the dielectric constant before polarisation is 23.46 for the 0C sample and 23.72 for the 1C sample, while it is measured to be 26.68 for the 0C sample and 25.54 for the 1C sample after polarisation. The resonance behavior of permittivity can be explained with Lorentz model. According to Lorentz model, the permittivity is;

$$\varepsilon_r = 1 + \frac{\omega_p^2 (\omega_0^2 - \omega^2)}{(\omega_0^2 - \omega^2)^2 + \omega \omega_r^2} \tag{1}$$

where  $\omega_0 = 2\pi f_0$  is the characteristic frequency,  $\omega$  is angular frequency,  $\omega_{\tau}$  is a damping frequency, and  $\omega_p$  is the transverse frequency of lattice vibration. We can see in model and the figures, when  $\omega$  is less than  $\omega_0$ , permittivity is negative and samples show the inductive character (Z. Wang et al., 2020). The resonance behavior is observed because of the piezoelectric resonance effect of PAC (Yang et al., 2022).

Figure 1e and 1f shows the frequency dependent variation of the dielectric loss value of the samples before and after polarisation. We observed that negative dielectric loss values for the bigger frequency values than the resonance frequency. Negative dielectric loss means that the energy released is more than the energy absorbed (Axelrod et al., 2006). The peak values of dielectric loss at positive and negative resonance frequencies before polarisation are 459.6761 and -7552.6788 for 0C, and 4195.3025 and -244.2922 for 1C respectively, and after polarisation 2368.0796 and -191.2578 for 0C and 554.1878 and -883.5565 for 1C respectively.



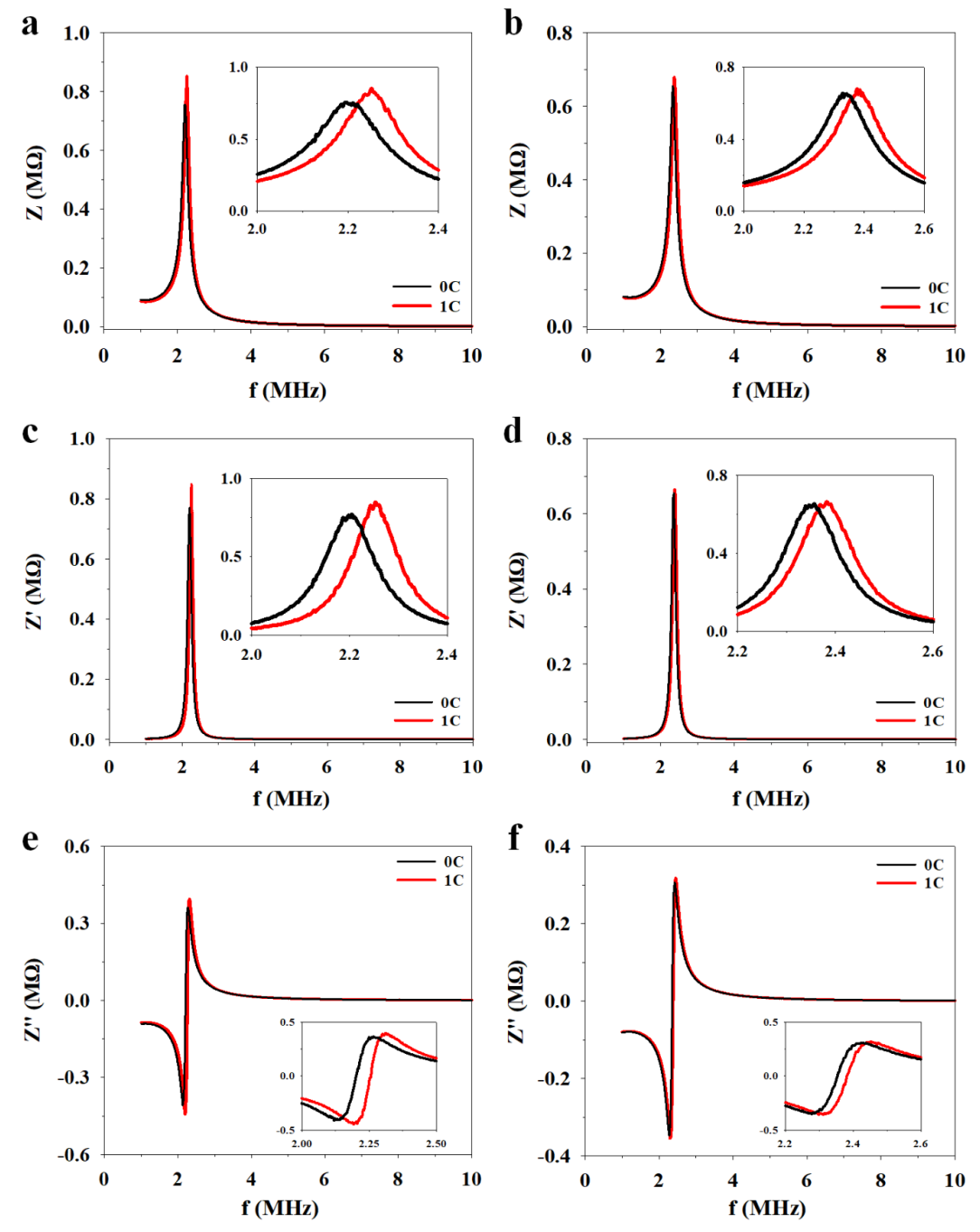
**Figure 1.** Frequency-dependent (a) capacitance, (c) permittivity, (e) dielectric loss, (g) dissipation factor before polarisation and (b) capacitance, (d) permittivity, (f) dielectric loss, (h) dissipation factor after polarisation measurements of 0C and 1C samples.

Figure 1g and 1h shows the frequency dependent variation of the dissipation factor value of the samples before and after polarisation. The dissipation factor is a parameter that indicates the amount of energy lost at a given frequency value

(Florkowski et al., 2024). It is equal to the ratio of the imaginary part of the dielectric permittivity to the real part  $(tan\delta = \varepsilon''/\varepsilon')$ . It can be seen that the dissipation factor reaches the highest values in the resonance frequency regions. 103.67 for 0C and

54.47 for 1C. The dissipation factor of 0C is higher than that of 1C (Figure 1g). After polarisation, the dissipation factor increases to 132.2 for 0C and 58.19 for 1C (Figure 1h). These values indicate that although polarisation increases the loss factor, this increase is much less than the rate of increase in permittivity and therefore it can be said that polarisation contributes positively to the permittivity of the film. It is noted that dissipation factor values of less than 5% are generally accepted as low dielectric loss (Z. Wang et al., 2020). The dissipation factor values outside the resonant frequency range

are very low in the measured frequency range. In general, there are polymers with very low loss values, but losses at 1 MHz frequency are up to 0.09 (Yu et al., 2008; Xu et al., 2013). In our study, this value is 0.0271 for the 0C before polarisation, 0.0197 for the 1C, 0.0266 for the 0C sample after polarisation and 0.0224 for the 1C sample. In the resonant frequency region, a high permeability frequency range can be obtained where the dielectric constant is negative and the dissipation factor is low. The characteristic situation in this region is very suitable for the realisation of metamaterial applications (Z. Wang et al., 2020).



**Figure 2.** Frequency-dependent (a) impedance, (c) resistance, (e) reactance, before polarisation and (b) impedance, (d) resistance, (f) reactance, after polarisation measurements of 0C and 1C samples.

Figure 2a shows the frequency variation of the impedance value of the samples before and after polarisation. At the resonance frequency, the impedance value takes the peak. The peak values are 0.7533 M $\Omega$  for the 0C and 0.8527 M $\Omega$  for the 1C before polarisation (Figure 2a). The impedance values after polarisation in Figure 2b are  $0.6375 \text{ M}\Omega$  for the 0C and 0.6797 $M\Omega$  for the 1C. A decrease in impedance values after polarisation is observed, and when the active carbon added, the peak of impedance value increased. While it is generally understood that active carbon enhances electrical conductivity and charge transfer capabilities, the specific interactions within the composite material, such as the distribution of active carbon within the polymer matrix and the formation of interfaces between carbon particles, can lead to unexpected impedance behaviour (Kozai et al., 2012; Cui et al., 2014). In the literature, we can see PMMA has the higher impedance values than PU and PAC. The impedance of pure PU measured above to  $10^4 \,\Omega$ at 1MHz and the impedance of Parylene C measured about 103  $\Omega$  at 0.1 MHz and see the frequency and impedance are inversely proportional (Kim & Cho, 2012; Chun et al., 2014). We can see the impedance of PMMA based doped conductive materials are about  $10^6 \Omega$  range at MHz frequencies (Shamrao et al., 2019). In our study, the impedance value of samples at 1 MHz are 0.07 and 0.09 M $\Omega$  band for all measurements. These values are close to literature.

Figure 2c and 2d shows that frequency dependent variation of the resistance value of the samples before and after polarisation. The peak values of resistance at the resonance frequency are 0.7706 M $\Omega$  for the 0C and 0.8473 M $\Omega$  for the 1C before polarisation (Figure 2c), and 0.6470 M $\Omega$  for the 0C and 0.6649 M $\Omega$  for the 1C after polarisation. (Figure 2d). After polarisation, we observed that a decrease in resistance values, and when the active carbon added, the peak of resistance value increased.

The frequency response of the reactance of the samples before and after polarisation is shown in Figure 2e and 2f. As expected, the reactance changes from negative to positive with a value of 0 due to the capacitive behaviour shown in Figure 1 and the inductive behaviour shown in the resonant frequency region. In the frequency range lower than the resonant frequency, the reactance takes a negative value and its absolute value decreases and approaches 0. This is caused by the capacitive behaviour of the material (Sun et al., 2019). In the range greater than the resonance frequency values, positive reactance, i.e. inductive character is observed. This is expressed by the formula  $Z''=Z_L+Z_C$  ( $Z_L=\omega L$  (inductive reactance),  $Z_C=1/\omega C$  (capacitive reactance)) (Z. Wang et al., 2020). The peak values of reactance before polarisation at the resonance frequency are 0.44 M $\Omega$  and -0.38 M $\Omega$  for 1C, 0.36 M $\Omega$  and - $0.40~\mathrm{M}\Omega$  for 0C, respectively. The peak values of reactance after polarisation at the resonance frequency are 0.31 M $\Omega$  and -0.35 M $\Omega$  for the 1C, 0.30 M $\Omega$  and -0.35 M $\Omega$  for the 0C, respectively.

#### 4. Conclusion

The dielectric properties of PAC-based composite films are investigated as a function of frequency using an impedance analyzer. This study examines the effects of activated carbon doping and the polarization process on the composite films. Negative capacitance and negative dielectric permittivity are observed through dielectric resonance The analysis of the PACbased composite films reveals an inductive character at frequencies surpassing the resonance frequency. Upon polarization, the samples exhibit a notable increase in capacitance and dielectric constant, coupled with a reduction in impedance. Interestingly, the incorporation of activated carbon introduces an unexpected phenomenon: a heightened impedance peak. This observation, however, is accompanied by a moderate increase in dielectric losses. Despite this increase in losses, the overall effect of polarization remains positive, as the gains in capacitance and dielectric constant significantly outweigh the losses. Furthermore, within a specific frequency range, the composite films display remarkable properties characterized by negative capacitance, high permittivity, and low dielectric losses. This unique combination of properties holds potential for various applications in advanced electronic devices and energy storage systems. The observed negative capacitance, in particular, suggests the possibility of enhancing charge storage capabilities beyond traditional limits.

In conclusion, this study highlights the intricate relationship between polarization, activated carbon doping, and the dielectric properties of PAC-based composite films. While the addition of activated carbon introduces a trade-off between impedance and losses, the overall impact of polarization on capacitance and dielectric constant remains favorable. The discovery of negative capacitance within a specific frequency range opens up new avenues for exploring innovative materials with tailored dielectric properties. Further investigations into the underlying mechanisms responsible for these observations may lead to the development of advanced materials with enhanced performance for various technological applications. This frequency range holds potential for various metamaterial applications. However, due to the inherently low permittivity of the polymers employed, their utilization in applications demanding high permittivity may present limitations in terms of efficiency and performance.

#### Acknowledgment

This work was financially supported by the funds of The Scientific and Technological Research Council of Turkey (TUBITAK) (120M636) and Kastamonu University—Turkey research Grant (KUBAP-01/2022-28).

#### **Conflict of Interest**

The authors declare that they have no conflict of interest.

#### References

- Axelrod, E., Puzenko, A., Haruvy, Y., Reisfeld, R., & Yuri Feldman Y. (2006). Negative dielectric loss phenomenon in porous sol–gel glasses. *Journal of Non-Crystalline Solids*, 352(40-41), 4166-4173. https://doi.org/10.1016/j.jnoncrysol.2006.07.008
- Balu, S. K., Shanker, N. P., Manikandan, M., Aparnadevi, N., Mulikraj, T., Manimuthu, P., & Venkateswaran, C. (2020). Crossover to negative dielectric constant in perovskite PrMnO<sub>3</sub>. *Physica Status Solidi A-Applications and Materials Science*, 217(17), 2000230. <a href="https://doi.org/10.1002/pssa.202000230">https://doi.org/10.1002/pssa.202000230</a>
- Chun, W., Chou, N., Cho, S., Yang, S., & Kim, S. (2014). Evaluation of sub-micrometer parylene C films as an insulation layer using electrochemical impedance spectroscopy. *Progress in Organic Coatings*, 77(2), 537-547. <a href="https://doi.org/10.1016/j.porgcoat.2013.11.020">https://doi.org/10.1016/j.porgcoat.2013.11.020</a>
- Cui, W., Cheng, N., Liu, Q., Ge, C., Asiri, A. M., & Sun, X. (2014). Mo<sub>2</sub>C nanoparticles decorated graphitic carbon sheets: Biopolymer-derived solid-state synthesis and application as an efficient electrocatalyst for hydrogen generation. *Acs Catalysis*, 4(8), 2658-2661. <a href="https://doi.org/10.1021/cs5005294">https://doi.org/10.1021/cs5005294</a>
- Dong, J., Li, L., Qiu, P., Pan, Y., Niu, Y., Sun, L., Pan, Z., Liu, Y., Tan, L., Xu, X., Luo, G., & Wang, H. (2023). Scalable polyimide-organosilicate hybrid films for high-temperature capacitive energy storage. *Advanced Materials*, 35(20), 2211487. <a href="https://doi.org/10.1002/adma.202211487">https://doi.org/10.1002/adma.202211487</a>
- El-Nahass, M. M., Attia, A. A., Salem, G. F., Ali, H. A. M., & Ismail, M. I. (2014). Dielectric and impedance spectral characteristics of bulk ZnIn<sub>2</sub>Se<sub>4</sub>. *Physica B: Condensed Matter*, 434, 89-94. <a href="https://doi.org/10.1016/j.physb.2013.10.049">https://doi.org/10.1016/j.physb.2013.10.049</a>
- Florkowski, M., Kuniewski, M., & Mikrut P. (2024). Effect of voltage harmonics on dielectric losses and dissipation factor interpretation in high-voltage insulating materials. *Electric Power Systems Research*, 226, 109973. https://doi.org/10.1016/j.epsr.2023.109973
- Hoffmann, M., Fengler, F. G. P., Herzig, M., Mittmann, T. M. B., Schroeder, U., Negrea, R. L. P., Slesazeck, S., & Mikolajick, T. (2019). Unveiling the double-well energy landscape in a ferroelectric layer. *Nature*, *565*, 464-467. <a href="https://doi.org/10.1038/s41586-018-0854-z">https://doi.org/10.1038/s41586-018-0854-z</a>
- Hu, Z., Liu, X., Ren, T., Saeed, H. A. M, Wang, Q., Cui, X., Huai, K., Huang, S., Xia, Y., Fu, K., Zhang, J., & Chen, Y. (2022). Research progress of low dielectric constant polymer materials. *Journal of Polymer Engineering*, 42(8), 677-687. <a href="https://doi.org/10.1515/polyeng-2021-0338">https://doi.org/10.1515/polyeng-2021-0338</a>
- Íñiguez, J., Zubko, P., Luk'yanchuk, I., & Cano, A. (2019). Ferroelectric negative capacitance. *Nature Reviews Materials*, *4*, 243-256. <a href="https://doi.org/10.1038/s41578-019-0089-0">https://doi.org/10.1038/s41578-019-0089-0</a>

- Jiang, W., Hardy, D. J., Phillips, J. C., MacKerell, A. D., Schulten, K., & Roux, B. (2010). High-performance scalable molecular dynamics simulations of a polarizable force field based on classical drude oscillators in namd. *The Journal of Physical Chemistry Letters*, 2(2), 87-92. <a href="https://doi.org/10.1021/jz101461d">https://doi.org/10.1021/jz101461d</a>
- Jones, B. K., Santana, J., & McPherson, M. (1998). Negative capacitance effects in semiconductor diodes. *Solid State Communications*, 107(2), 47-50. https://doi.org/10.1016/S0038-1098(98)00162-8
- Kahouli, A., Sylvestre, A., Ortega, L., Jomni, F., Yangui, B., Maillard, M., Berge, B., Robert, J. C., & Legrand J. (2009). Structural and dielectric study of parylene C thin films. *Applied Physics Letters*, *94*(15), 152901. https://doi.org/10.1063/1.3114404
- Khan, A. I., Chatterjee, K., Wang, B., Drapcho, S., You, L., Serrao, C., Bakaul, S. R., Ramesh, R., & Salahuddin, S. (2015). Negative capacitance in a ferroelectric capacitor. *Nature Materials*, 14(2), 182-186. <a href="https://doi.org/10.1038/nmat4148">https://doi.org/10.1038/nmat4148</a>
- Kim, S., & Cho, S. (2012). Parylene-C-coated indium tin oxide electrodes for the optical-and electrical-impedance characterization of cells. *Journal of Nanoscience and Nanotechnology*, 12(7), 5830-5834. https://doi.org/10.1166/jnn.2012.6363
- Kozai, T. D. Y., Langhals, N. B., Patel, P. R., Deng, X., Zhang, H., Smith, K., Lahann, J., Kotov, N. A., & Kipke, D. R. (2012). Ultrasmall implantable composite microelectrodes with bioactive surfaces for chronic neural interfaces. *Nature Materials*, 11(12), 1065-1073. <a href="https://doi.org/10.1038/nmat3468">https://doi.org/10.1038/nmat3468</a>
- Kurnaz, S., Ozturk, O., Hazar, M. A., Guduloglu, U., Yilmaz, N., & Cicek, O. (2023). Flexible capacitive and piezoresistive pressure sensors based on screen-printed parylene C/polyurethane composites in low-pressure range. Flexible and Printed Electronics, 8(3), 035015. <a href="https://doi.org/10.1088/2058-8585/acf774">https://doi.org/10.1088/2058-8585/acf774</a>
- Leng, Z., Wu, H., Tang, X., Li, Y., Xin, Y., Xie, P., Li, G., Yan, K., & Liu, C. (2020). Carbon nanotube/epoxy composites with low percolation threshold and negative dielectric constant. *Journal of Materials Science: Materials in Electronics*, 33, 26015-26024. https://doi.org/10.1007/s10854-022-09291-6
- Li, H., Ai, D., Ren, L., Yao, B., Han, Z., Shen, Z., Wang, J., Chen, L., & Wang, Q. (2019). Scalable polymer nanocomposites with record high-temperature capacitive performance enabled by rationally designed nanostructured inorganic fillers. *Advanced Materials*, 31(23), 1900875. https://doi.org/10.1002/adma.201900875
- Liu, Y., Xu, C., Ren, H., Wei, Z., & Zhang, Z. (2020). Tailorable negative permittivity in Fe/BaTiO<sub>3</sub> metacomposites. *Functional Materials Letters*, *13*(03), 2050017. https://doi.org/10.1142/S1793604720500174

- Mokni, M., Maggioni, G., Kahouli, A., Carturan, S. M., Raniero, W., & Sylvestre, A. (2019). Nanocomposite—parylene C thin films with high dielectric constant and low losses for future organic electronic devices. *Beilstein Journal of Nanotechnology*, *10*, 428-441. https://doi.org/10.3762/bjnano.10.42
- Oughstun, K. E., & Cartwright, N. A. (2003). On the lorentz-lorenz formula and the lorentz model of dielectric dispersion. *Optics Express*, 11(13), 1541-1546. <a href="https://doi.org/10.1364/oe.11.001541">https://doi.org/10.1364/oe.11.001541</a>
- Qu, Y., Du, Y., Fan, G., Xin, J., Liu, Y., Xie, P., You, S., Zhang, Z., Sun, K., & Fan, R. (2019). Low-temperature sintering Graphene/CaCu<sub>3</sub>Ti<sub>4</sub>O<sub>12</sub> nanocomposites with tunable negative permittivity. *Journal of Alloys and Compounds*, 771, 699-710. <a href="https://doi.org/10.1016/j.jallcom.2018.09.049">https://doi.org/10.1016/j.jallcom.2018.09.049</a>
- Raja, V., Sharma, A. K., & Rao, V. V. R. N. (2004). Impedance spectroscopic and dielectric analysis of PMMA-CO-P<sub>4</sub>VPNO polymer films. *Materials Letters*, *58*(26), 3242-3247. <a href="https://doi.org/10.1016/j.matlet.2004.05.061">https://doi.org/10.1016/j.matlet.2004.05.061</a>
- Romano, S., Cabrini, S., Rendina, I., & Mocella, V. (2014). Guided resonance in negative index photonic crystals: A new approach. *Light: Science &Amp; Applications*, 3(1), e120. https://doi.org/10.1038/lsa.2014.1
- Sankar, S., Kanagathara, N., & Robinson Azariah, J. C. (2022). Electric modulus, dielectric relaxation mechanism and impedance properties of melaminum perchlorate monohydrate broadband dielectric spectroscopic study. *Acta Physica Polonica A*, 141(5), 500-506. <a href="https://doi.org/10.12693/APhysPolA.141.500">https://doi.org/10.12693/APhysPolA.141.500</a>
- Shamrao, P. V., Vithya, K., Premalatha, M., & Sundaresan, B. (2019). AC impedance study of PMMA-LiNO<sub>3</sub> electrolyte. *In Macromolecular Symposia*, 387(1), 1800187. <a href="https://doi.org/10.1002/masy.201800187">https://doi.org/10.1002/masy.201800187</a>
- Sun, K., Dong, J., Wang, Z., Wang, Z., Fan, G., Hou, Q., An, L., Dong, M., Fan, R., & Guo, Z. (2019). Tunable negative permittivity in flexible graphene/PDMS metacomposites. *The Journal of Physical Chemistry*, *123*(38), 23635-23642. https://doi.org/10.1021/acs.jpcc.9b06753
- Vandeparre, H., Watson, D., & Lacour, S. P. (2013). Extremely robust and conformable capacitive pressure sensors based on flexible polyurethane foams and stretchable metallization. *Applied Physics Letters*, 103(20), 204103. <a href="https://doi.org/10.1063/1.4832416">https://doi.org/10.1063/1.4832416</a>
- Wang, D., Li, H., Li, M., Jiang, H., Xia, M., & Zhou, Z. (2013). Stretchable conductive polyurethane elastomer in situ polymerized with multi-walled carbon nanotubes.

- Journal of Materials Chemistry C, 1(15), 2744-2749. https://doi.org/10.1039/C3TC30126E
- Wang, T., Liu, S., Li, X., Wang, Q., Liu, S., Liang, X., Li, S., Liu, B., Liu, J., & Zhang, G. (2022). Wide bandgap nanocoatings for polymer dielectric with outstanding electrical strength. *Advanced Materials Interfaces*, *9*(35), 2201824. https://doi.org/10.1002/admi.202201824
- Wang, Z., Li, H., Hu, H., Fan, Y., Fan, R., Li, B., Zhang, J., Liu, H., Fan, J., Hou, H., Dang, F., Kou, Z., & Guo Z. (2020). Direct observation of stable negative capacitance in SrTiO<sub>3</sub>@ BaTiO<sub>3</sub> heterostructure. *Advanced Electronic Materials*, 6(2), 1901005. https://doi.org/10.1002/aelm.201901005
- Wong, J. C., & Salahuddin S. (2018). Negative capacitance transistors. *Proceedings of the IEEE*, 107(1), 49-62. https://doi.org/10.1109/JPROC.2018.2884518
- Xie, P., Shi, Z., Feng, M., Sun, K., Liu, Y., Yan, K., Liu, C., Moussa, T. A. A., Huang, M., Meng, S., Liang, G., Hou, H., Fan, R., & Guo, Z. (2022). Recent advantages in radio-frequency negative dielectric metamaterials by designing heterogeneous composites. *Advanced Composites and Hybrid Materials*, 5, 679-695. https://doi.org/10.1007/s42114-022-00479-2
- Xu, J., Zhu, L., Fang, D., Liu, L., Wang, L., & Xu, W. (2013).
  Prediction of dielectric dissipation factors of polymers from cyclic dimer structure using multiple linear regression and support vector machine. *Colloid and Polymer Science*, 291, 551-561.
  <a href="https://doi.org/10.1007/s00396-012-2743-6">https://doi.org/10.1007/s00396-012-2743-6</a>
- Yan, H., Zhao, C., Wang, K., Deng, L., Ma, M., & Xua, G. (2013). Negative dielectric constant manifested by static electricity. *Applied Physics Letters*, 102, 062904. https://doi.org/10.1063/1.4792064
- Yang, P., Sun, K., Wu, Y., Wu, H., Yang, X., Wu, X., Du, H., & Fan, R. (2022). Negative permittivity behaviors derived from dielectric resonance and plasma oscillation in percolative bismuth ferrite/silver composites. *The Journal of Physical Chemistry C*, 126(30), 12889-12896. https://doi.org/10.1021/acs.jpcc.2c03543
- Yu, X., Yi, B., Liu, F., & Wang, X. (2008). Prediction of the dielectric dissipation factor tanδ of polymers with an ANN model based on the DFT calculation. *Reactive & Functional Polymers*, 68(2008), 1557-1562. https://doi.org/10.1016/j.reactfunctpolym.2008.08.009

#### AIMS & SCOPE

Journal of Advanced Applied Sciences aims to publish relevant articles that focus on modern applications of Physics, Electrical and Electronics Engineering, Computer Science and Information Engineering and Material Science. We are particularly interested in applied research that makes significant scientific contributions across the broad spectrum of applied sciences.

The Physics and Materials section of the Journal of Advanced Applied Sciences targets the latest development in the Applied Physics area and its intersection with the Material Science. Some keywords that we are considering are: Electronic properties of materials, Optical properties of materials, Mechanical properties of materials, Magnetic properties of materials and Structural properties of materials. Structure-Property relationship Especially, characterization, Superconductivity, Cryogenics, Semiconductivity, Spintronics, Organic electronics, Perovskite/ Silicon solar cells, Biomaterials and health applications, Bioelectronics and sensors, Photonic Thermoelectric Nanomaterials/nanoparticles, Energy transfer storage and conversion, Organic materials doping, Batteries, Alloys and ceramics, Applied biophysics and other topics related to applied sciences.

The **Engineering section** deals with studies in various sub-disciplines of electrical and electronics and computer engineering technology such as Applied Engineering, Robotics and Control, Signal Processing, Data Analysis, Computational Systems, Communication Systems, Machine Learning, Artificial Intelligence and Deep Learning, Image Processing and Signal Processing, Big Data, Energy, Power and Industrial Applications, Systems security and data encryption, Microwaves and optics.

#### **AUTHOR GUIDELINES**

Manuscripts must be submitted to the journal in electronic version through online submission system at <a href="https://prensipjournals.com/ojs/index.php/jaasci/author-guidelines">https://prensipjournals.com/ojs/index.php/jaasci/author-guidelines</a> following the Author Guidelines of the journal.

#### **Types of Paper**

Research articles, review articles, short communications, and letters to the Editor.

- Research articles: original full-length research papers which have not been published previously and should not exceed 7500 words or 25 manuscript pages (including tables and figures).
- Review articles: on topical subjects and up to 10000 words or 25 manuscript pages (including tables and figures).
- Short communications: describing work that may be of a preliminary nature or a case report; preferably no more than 3000 words or 10 manuscript pages (including tables and figures).

• Letters to the Editor: should be included on matters of topical interest and not exceeding 2000 words or 10 manuscript pages (including tables and figures).

#### **Page Charges**

This journal has no page charges.

#### **Preparation of Manuscripts**

Papers must be written in English. Prepare your text using a word-processing software and save in ".doc" or ".docx" formats. Manuscripts must be structured in the following order:

#### • Title Page File

- Title (Concise and informative. Avoid abbreviations and formulae)
- Author names and affiliation addresses (Full names should be given, no abbreviations. The corresponding author should be identified with an asterisk. Each affiliation address should include institution, faculty/school, department, city, and country)
- ORCID numbers for all authors.
- Corresponding author's e-mail, telephone number, and address
- Acknowledgements (if applicable. Keep these to the absolute minimum)
- Compliance with Ethical Standards
  - Conflict of Interest Statement
  - Statement on the Welfare of Animals (if applicable)
  - Statement of Human Rights (if applicable)

#### • Main File

- Title
- Abstract (Should be between 100 and 350 words.
   References and abbreviations should be avoided)
- Keywords (Minimum 3, Maximum 6 keywords)
- Introduction
- Materials and Methods
- Results
- Discussion (Can be combined with Results section if appropriate)
- Conclusion
- References
- Table(s) with caption(s) (on appropriate location in the text)
- Figure(s) with caption(s) (on appropriate location in the text)
- and appendices (if any)

#### **Manuscript Formatting**

Use a 12-point Times New Roman font, including the references, table headings and figure captions, double-spaced and with 25 mm margins on all sides of A4 size paper throughout the manuscript. The text should be in single-column format.

• Each page must be numbered with Arabic numerals, and lines must be continuously numbered from the start to the end of the manuscript.



- Use italics for emphasis.
- Use only SI (international system) units.
- Use "dot" for decimal points.

#### References

Journal of Advanced Applied Sciences uses APA style (7th edition). Accordingly, authors must format their references as per the guidelines below. Please ensure that each reference cited in the text is also presented in the reference list. Authors should always supply DOI or URL of the work cited if available.

#### In-text citation (Narrative):

- ... The results of Bliss (2022) support...
- ...Sönmez and Taştan (2020) indicated that...
- ...According to the method of Öztürk et al. (2021)...

#### In-text citation (In parenthesis):

- ...It was found to be isometric (Öztürk, 2018)...
- ...is highly susceptible to friction (Doma & Craig, 2019)...
- ...have been studied (Kale et al., 2020)...

#### Two or more works in the same parenthesis:

...crushes under high pressure (Sönmez, 2018, 2019; Öztürk et al., 2020a; Kadak & Taştan, 2021)...

#### Citation in the reference list:

References should be listed first alphabetically and then further sorted chronologically at the end of the article. The citation of all references should conform to the following examples:

#### Article:

- Lastname, N., Lastname, M., & Lastname, O. (Year). Title of the work. *Title of the Journal*, *Volume*(Issue), Page numbers. DOI
- Tort, S. (1998). Stress and immune modulation in fish. Developmental & Comparative Immunology, 35(12), 1366-1375. https://doi.org/10.1016/j.dci.2011.07.002
- Kasumyan, A. O., & Døving, K. B. (2003). Taste preferences in fishes. *Fish and Fisheries*, *4*(4), 289-347. https://doi.org/10.1046/j.1467-2979.2003.00121.x
- Özçelik, H., Taştan, Y., Terzi, E., & Sönmez, A. Y. (2020). Use of onion (*Allium cepa*) and garlic (*Allium sativum*) wastes for the prevention of fungal disease (*Saprolegnia parasitica*) on eggs of rainbow trout (*Oncorhynchus mykiss*). *Journal of Fish Diseases*, 43(10), 1325-1330. https://doi.org/10.1111/jfd.13229

#### Article by DOI (early access):

Salem, M. O. A., Salem, T. A., Yürüten Özdemir, K., Sönmez, A. Y., Bilen, S., & Güney, K. (2021). Antioxidant enzyme activities and immune responses in rainbow trout (*Onchorhynchus mykiss*) juveniles fed diets supplemented with dandelion (*Taraxacum officinalis*) and lichen (*Usnea barbata*) extracts. *Fish Physiology and Biochemistry*. https://doi.org/10.1007/s10695-021-00962-5

#### Book:

- Lastname, N., Lastname, M., & Lastname, O. (Year). *Title of the work.* Publisher.
- Oidtmann, K., Xao, Q., & Lloyd, A. S. (2018). *The food need by the year 2050*. Elsevier.

#### **Book Chapter:**

- Lastname, N., Lastname, M., & Lastname, O. (Year).

  Title of the chapter. In N. N. Lastname, A. Lastname & B. Lastname (Eds.), *Title of the book* (pp. Page numbers). Publisher.
- Pickering, A. D. (1993). Growth and stress in fish production. In G. A. E. Gall & H. Chen (Eds.), *Genetics in Aquaculture* (pp. 51-63). Elsevier. https://doi.org/10.1016/b978-0-444-81527-9.50010-5

#### **Dissertation or Thesis:**

- Lastname, N. (Year). *Title of dissertation/thesis* (Doctoral dissertation/Master's thesis, Name of Institution).
- Sönmez, A. Y. (2011). Karasu ırmağında ağır metal kirliliğinin belirlenmesi ve bulanık mantıkla değerlendirilmesi (Doctoral dissertation, Atatürk University).
- Taştan, Y. (2018). Tatlısu kerevitindeki (Astacus leptodactylus) siyah solungaç hastalığı etkeni mantar Fusarium oxysporum'un PCR yöntemi ile teşhisi (Master's thesis, Akdeniz University).

#### Conference Proceedings:

- Lastname, N., Lastname, M., & Lastname, O. (Year). *Title of the work.* Title of the Conference. City.
- Ken, A., & Kumar, S. (2020). *A new statistical model* for fuzzy logic evaluation. 3<sup>rd</sup> International Congress on Statistics. İstanbul.

#### Institution Publication:

Institution name. (Year). Title of the work. URL

FAO. (2020). Fishery and aquaculture statistics 2018. http://www.fao.org/3/cb1213t/CB1213T.pdf

#### **Internet Source:**

- Lastname, N. (Year). *Title of the work*. Retrieved May 15, 2020, from URL
- Perreault, L. (2019). *The future of agriculture: Polyculture*. Retrieved January 12, 2020, from https://www.agriculture.com

#### Table(s)

Tables, numbered in Arabic, should be in separate pages with a short descriptive title at the top. Place footnotes to tables below the table body and indicate them with superscript lowercase letters (or asterisks for significance values and other statistical data).

#### Figure(s)

All illustrations should be labelled as 'Figure' and numbered in consecutive Arabic numbers, Figure 1, Figure 2 etc. in the text. If panels of a figure are labelled (a, b, etc.) use the same case when referring to



these panels in the text. Figures are recommended to be in electronic formats such as PNG, JPEG, TIFF (min. 300 dpi). All figures or tables should be presented in the body of the text.

#### **Online Manuscript Submission**

Authors are requested to submit manuscripts via the journal's online submission system at <a href="https://prensipjournals.com/ojs/index.php/jaasci/index">https://prensipjournals.com/ojs/index.php/jaasci/index</a>

#### **Submission Checklist**

o Author Guidelines of the journal has been read and adhered

#### • Title Page File

- o Title
- Full names, e-mails, and affiliation addresses of all authors
- ORCID numbers of all authors
- o Corresponding author's e-mail, telephone number, and address
- o Ethical statements

#### • Main File

- o Continuous page numbers
- o Continuous line numbers
- o Blinded document (no personal information is present)
- o Title
- O Abstract (100-350 words)
- Keywords (3-6 keywords)
- o All figures and tables are numbered and cited in order in text
- o Completeness and accuracy of the references have been checked
- o References have been edited as per the Journal guidelines

#### **Publication Frequency**

The journal includes original scientific articles on a variety of different subjects in English and is being published twice a year in June and December.

#### **Publication Fees**

*Journal of Advanced Applied Sciences* is an open access journal. No submission or publication charges are collected. All authors and readers have free access to all papers.

#### **PUBLICATION ETHICS**

Details about Publication Ethics can be found at https://prensipjournals.com/ojs/index.php/jaasci/policy

#### OPEN ACCESS POLICY

Details can be found at

https://prensipjournals.com/ojs/index.php/jaasci/openaccess

#### REVIEW PROCESS

#### **Double-Blind Review and Evaluation Process**

Double-Blind Review is a method applied for publishing scientific publications with the highest

quality. This method forms the basis of an objective evaluation of scientific studies and is preferred by many scientific journals.

The views of referees have a decisive place in the publication quality of a Journal. *Journal of Advanced Applied Sciences* uses the double-blind review method, which means that both the reviewer and author identities are concealed from the reviewers, and vice versa, throughout the review process, in the evaluation process of all studies. For this reason, the authors are asked to blind their manuscripts before submitting. All the studies submitted to *Journal of Advanced Applied Sciences* are evaluated by double-blind review method according to the following steps.

#### 1. Initial Evaluation Process

The studies submitted to *Journal of Advanced Applied Sciences* are first evaluated by the editor. At this stage, studies that are not in line with the aim and scope of the journal, are weak in terms of language and narrative rules in English, contain scientifically critical mistakes, are not original worthy, and cannot meet publication policies are rejected. Authors of rejected studies will be notified within one month at the latest from the date of submission. Eligible studies are sent to the field editor to which the study is relevant for preevaluation.

#### 2. Pre-Evaluation Process

In the pre-evaluation process, the field editors examine the studies, introduction and literature, methods, findings, results, evaluation and discussion sections in detail in terms of journal publication policies, scope and authenticity of study. Study which is not suitable as a result of this examination is returned to the author with the field editor's evaluation report within four weeks at the latest. The studies which are suitable for the journal are passed to the referee process.

#### 3. Referee Process

The studies are sent to the referees according to their content and the expertise of the referees. The field editor examining the study may propose at least two referees from the pool of *Journal of Advanced Applied Sciences* Advisory Board or referee pool according to their field of expertise or may propose a new referee appropriate to the field of study. The editors evaluate the referee's suggestions coming from the field editor and the studies are submitted to the referees. Referees are obliged to guarantee that they will not share any process or document about the study they are evaluating.

#### 4. Referee Evaluation Process

The period given to the referee for the evaluation process is 15 days. Proposals for corrections from referees or editors must be completed by the authors within 1 month according to the "correction instruction". Referees can decide on the suitability of the study by reviewing the corrections and may also request multiple corrections if necessary.



#### **Referee Reports**

Referee evaluations are based in general on the originality of the studies, the method used, and the conformity with the ethical rules, the consistent presentation of the findings and results, and the examination of the literature.

This review is based on the following elements:

- 1. Introduction and Literature: The evaluation report contains the presentation and purpose of the problem addressed in the study, the importance of the topic, the scope of the relevant literature, the timeliness and the originality of the study.
- 2. Methodology: The evaluation report includes information on the suitability of the method used, the choice and characteristics of the research group, validity and reliability, as well as on the data collection and analysis process.
- 3. Findings: The evaluation report includes opinions on the presentation of the findings obtained in the frame of the method, the correctness of the analysis methods, the aims of the research and the consistency of the findings, the presentation of the required tables, figures and images and the conceptual evaluation of the tests used
- 4. Evaluation and discussion: The evaluation report includes the opinion on the subject based on findings, relevance to research questions and hypotheses, generalizability and applicability.
- 5. Conclusion and suggestions: The evaluation report contains the opinion on the contributions to the literature, future studies and recommendations for the applications in the area.
- 6. Style and narration: The evaluation report includes compatibility of the title with the content, appropriate use of English in the study, refers and references in accordance with the language of the study and APA rules.
- 7. Overall evaluation: The evaluation report contains opinion on the authenticity of the study as a whole, its contribution to the educational literature and the applications in the area. The journal considers that scientists should avoid research which kills or damages any species of animal which, using IUCN criteria, is regarded as threatened or is listed as such in a Red Data Book appropriate for the geographic area concerned. In accordance with this view, papers based on such research will not be accepted by the Journal, unless the work had clear conservation objectives.

#### **Plagiarism Detection**

In agreement with publishing policies of *Journal of Advanced Applied Sciences*, plagiarism check is required for each study that has undergone the "Review Process". The Turnitin plagiarism checker software is used for plagiarism detection.

#### Proofs

Proof documents will be sent to the corresponding authors via e-mail. Proofs should be checked immediately and responses should be returned back within 15 working days. It is the responsibility of the authors to check carefully the proofs. No changes will be allowed after this stage.

#### **DISCLAIMER**

The Publisher and Editors cannot be held responsible for errors or any consequences arising from the use of information contained in this journal; the views and opinions expressed do not necessarily reflect those of the Publisher and Editors.

Editor or members of the editorial board are not responsible for the author's opinions and manuscript contents. Authors are responsible for the ethical originality of and possible errors in their manuscripts.

This journal is available online at http://jaasci.com/

Kindly visit website to search the articles and register for table of contents e-mail alerts.

#### LICENCE

Authors retain copyright and grant the journal right of first publication with the work simultaneously licensed under a Creative Commons Attribution License that allows others to share the work with an acknowledgement of the work's authorship and initial publication in this journal.

Authors are able to enter into separate, additional contractual arrangements for the non-exclusive distribution of the journal's published version of the work (e.g., post it to an institutional repository or publish it in a book), with an acknowledgement of its initial publication in this journal.

Authors are permitted and encouraged to post their work online (e.g., in institutional repositories or on their website) prior to and during the submission process, as it can lead to productive exchanges, as well as earlier and greater citation of published work (See The Effect of Open Access).

#### **INDEXING**

Journal of Advanced Applied Sciences is currently indexed by

- Crossref
- Scilit
- Index Copernicus
- EuroPub
- Road
- Google Scholar

#### **PUBLISHER**



Prensip Publishing and Consultancy Ind. Trade. Co. Ltd. Kuzeykent mah., Orgeneral Atilla Ateş Paşa Cad., No: 15CD, İç Kapı No:31, Merkez/Kastamonu, 37150, TÜRKİYE

> https://prensip.gen.tr info@prensip.gen.tr



